Double-differential Measurements of Mesonless Charged-current Muon Neutrino Interactions on Argon with Final-State Protons using the MicroBooNE Detector

The MicroBooNE Collaboration*

September 8, 2021

Contents

---

*MICROBOONE_INFO@fnal.gov

1 Introduction

This note reports the first double-differential measurements of charged-current ν_μ scattering on argon leading to final states containing zero mesons and one or more protons. This event topology (hereafter abbreviated as CC0πNp) is the most common at the neutrino energies typically produced by the Fermilab Booster Neutrino Beam. A detailed understanding of neutrino-argon scattering in the CC0πNp channel is therefore crucial for the success of the precision neutrino oscillation analyses planned for the Short-Baseline Neutrino (SBN) program [1]. This remains true for the upcoming Deep Underground Neutrino Experiment (DUNE) [2], but the higher mean neutrino energy used there will ensure that more inelastic reaction modes, such as single pion production, will also play a major role.

The analysis described in this note builds on a previous MicroBooNE study of the CC0πNp channel [3] which obtained the first single-differential cross-section measurements on an argon target. Since that foundational work, significant improvements have been made to MicroBooNE's simulation software, event reconstruction algorithms, and procedure for calculating systematic uncertainties. When combined with a larger dataset (corresponding to a beam exposure of 6.79×10^{20} protons-on-target versus 1.60×10^{20} in Ref. [3]), these enhancements allow the important CC0πNp channel to be studied in more detail.

This note begins with a description of the data and simulation samples used as input to the analysis. Section 3 then defines the CC0πNp signal event topology, and Section 4 describes a set of selection criteria designed to identify these events in MicroBooNE data. Binning schemes are then defined in Section 5 for two double-differential measurements of event rates. The first of these considers the momentum and scattering cosine of the outgoing muon, while the second reports the same observables for the leading proton, i.e., the final-state proton with the largest momentum. After a discussion of systematic uncertainties in Section 6, the note concludes by comparing the predictions of MicroBooNE Monte Carlo (MC) simulations to the measured double-differential distributions.

These results will form the basis for a future extraction of flux-averaged double-differential CC0πNp cross sections that will be immediately comparable to the theoretical predictions of multiple neutrino event generators. The selection described herein may also be used to study various other observables in CC0πNp events, including those which are sensitive to correlations between leptonic and hadronic kinematics in the final state.

2 Datasets and Monte Carlo simulations

The measurements described in this note are obtained using MicroBooNE datasets recorded during the entirety of Runs 1–3. Two categories of data are used. The *beam-on* data samples were taken when the Fermilab Booster Neutrino Beam (BNB) was active and correspond to a total exposure of 6.79×10^{20} protons-on-target (POT). The *beam-off* data were recorded during time intervals outside of the beam window or when the beam was shut down altogether. These data allow for a direct measurement of backgrounds generated by cosmic rays and other constant-in-time sources (e.g., natural radioactivity).

To preserve blindness for MicroBooNE's ongoing analyses investigating the MiniBooNE electron-like low-energy excess [4], information about all variables specific to ν_e measurements were removed from the beam-on data samples at the time of processing.

Data or MC sample	DAQ triggers	Beam exposure (POT)
Beam-on data	159,197,948	6.79×10^{20}
Beam-off data	432,458,871	N/A
Central-Value MC	N/A	3.66×10^{21}
Intrinsic ν_e MC	N/A	1.93×10^{23}
Dirt MC	N/A	1.60×10^{21}
DetVar1 MC	N/A	1.24×10^{21}
DetVar2 MC	N/A	6.13×10^{20}

Table 1: Data and Monte Carlo simulation samples analyzed to obtain the results reported in this note.

Monte Carlo simulations of neutrino interactions in the MicroBooNE detector are used in this analysis to develop the event selection, estimate efficiencies and beam-correlated backgrounds, and assess systematic uncertainties. The G18_10a_02_11a configuration of version 3.0.6 of the GENIE neutrino event generator [5] is used to simulate neutrino scattering events. These are subsequently reweighted to adjust four model parameters affecting the charged-current quasielastic (CCQE) and two-particle-two-hole (2p2h) cross sections. The new parameter values were determined by tuning the base GENIE model to a 2016 T2K cross-section dataset [6]. Further details about this *MicroBooNE GENIE tune* are available in Ref. [7].

The flux of incident neutrinos generated by the BNB is modeled in MicroBooNE simulations using a reimplementation of tools originally developed for the MiniBooNE experiment [8, 9]. The Geant4 toolkit [10] is used to simulate particle transport within and around the MicroBooNE detector. The response of the detector electronics to ionization and scintillation signals induced by the final-state particles is simulated using custom additions to LArSoft [11], a flexible software framework for liquid argon time projection chamber (LArTPC) experiments. LArSoft also provides a unified interface to the other simulation tools mentioned previously.

To account for backgrounds that overlap in time with beam neutrino interactions, MicroBooNE currently makes use of an *overlay* technique: simulated detector signals originating from neutrino scattering events produced by GENIE are superimposed on detector beam-off data. This approach represents an improvement over past MicroBooNE analyses (including the previous study of CC0πNp interactions [3]), which relied on the CORSIKA event generator [12] to model cosmic-ray backgrounds.

Table 1 lists the data and MC simulation samples used in the present analysis. A total number of triggers recorded by the data acquisition system (DAQ) is reported for data samples, and a total beam exposure (measured or simulated as appropriate) is reported for all but the beam-off data sample. Several categories of MC simulation samples are listed in the table, which are defined as follows:

CV Contains the primary simulated neutrino interactions used to form a central-value prediction of the expected event rates in the MicroBooNE detector. This sample is dominated by simulated ν_μ interactions, but other neutrino species are also present.

Intrinsic ν_e Contains simulated interactions arising from the intrinsic ν_e content of the BNB flux. Other neutrino species (including $\bar{\nu}_e$) are excluded. The large simulated beam exposure for this sample allows ν_e-induced backgrounds to be estimated with much reduced MC statistical uncertainties.

Dirt Includes simulated interactions of neutrinos of all flavors which occur outside of the MicroBooNE cryostat. These are distinct from the interactions in the previous two categories of MC samples, which are generated solely within the cryostat. Because the fiducial volume chosen as part of the signal definition for this analysis (see Section 3.1) lies entirely within the cryostat, all dirt events are considered background.

DetVar These *detector variation* samples use modifications of the default simulated detector response in order to calculate systematic uncertainties. To reduce MC statistical uncertainties in those calculations, a common set of GENIE events is reprocessed as input to modified simulations of the MicroBooNE detector response. Most of the detector variations are evaluated using a dedicated sample of events (DetVar1) corresponding to a simulated beam exposure of 1.24×10^{21} POT. However, two variations related to the treatment of space charge and ionization electron recombination are evaluated using a smaller MC sample (DetVar2) with a simulated beam exposure of 6.13×10^{20} POT. More details about the detector variations considered in this analysis are given in Section 6.4.

Normalization differences between the various samples listed in Table 1 are handled by scaling to the beam-on data. Event counts obtained from MC simulations are scaled by multiplying by the scale factor

$$S_{\mathrm{MC}} = \frac{\mathrm{POT}_{\mathrm{beam}}}{\mathrm{POT}_{\mathrm{MC}}} \qquad (1)$$

where $\mathrm{POT}_{\mathrm{beam}}$ is the measured beam exposure and $\mathrm{POT}_{\mathrm{MC}}$ is the simulated beam exposure for the MC sample of interest. A similar procedure based on the ratio of DAQ triggers is used to scale beam-off data samples. Specifically, beam-off event counts are multiplied by the scale factor

$$S_{\mathrm{off}} = \frac{\mathrm{DAQ}_{\mathrm{beam}}}{\mathrm{DAQ}_{\mathrm{off}}} \qquad (2)$$

where DAQ_{beam} is the number of DAQ triggers included in the beam-on data sample and DAQ_{off} is the number of DAQ triggers in the beam-off sample.

3 Signal definition

For the present analysis, a neutrino scattering event is considered part of the signal if it fulfills the following criteria:

(1) The true interaction vertex lies within the fiducial volume defined in Section 3.1

(2) A muon neutrino undergoes a charged-current interaction

(3) The final state contains at least one proton

(4) The true momentum of the outgoing muon is greater than 0.10 GeV/c

(5) The true momentum of the leading proton[1] lies within the interval [0.25, 1.2] GeV/c.

(6) The final state contains zero (anti)mesons.

The phase-space limits on the muon and leading proton momenta mentioned in signal requirements (4) and (5) are motivated by efficiency and resolution considerations. The specific values chosen are the same as in the previous MicroBooNE CC0πNp analysis [3] with one exception: the lower limit on the true leading proton momentum given in requirement (5) has been reduced from 0.30 GeV/c to 0.25 GeV/c. The motivation for this change is discussed in Section 4.4.

3.1 Fiducial volume

For this analysis, only events in which the true neutrino vertex falls within a designated *fiducial volume* are included in the signal definition. In the MicroBooNE detector coordinate system, the boundaries of the fiducial volume are defined by

$$21.50 \text{ cm} \leq x \leq 234.85 \text{ cm}$$
$$-95.00 \text{ cm} \leq y \leq 95.00 \text{ cm}$$
$$21.50 \text{ cm} \leq z \leq 966.80 \text{ cm}.$$

Figure 1 shows a schematic of the MicroBooNE detector with the fiducial volume used in this analysis drawn in green. The boundaries of the fiducial volume were chosen to provide a 21.50 cm border with the edges of the TPC active volume on all sides. The only exception to this is in the forward z direction. Here a 70 cm border is chosen to allow ample room for measurements of forward-going muon tracks.

For neutrino interactions occurring at the extreme edges of the fiducial volume, the chosen dimensions are sufficient for 0.50 GeV/c protons to be fully contained within the looser containment volume defined in Section 4.2. This helps to ensure good acceptance of low-momentum protons by the event selection described in Section 4.3, which requires the end points of all final-state particle tracks except the muon to lie within the containment volume. Forward muons and protons emerging from neutrino interactions at the downstream ($+z$) edge of the fiducial volume will remain inside the containment volume at momenta below 0.25 GeV/c and 0.85 GeV/c, respectively.

3.2 Event categories

Plots of event distributions shown in this note use a consistent color scheme and legend format. Although some effort is made to include a legend in the individual figures, Fig. 2 shows the legend that should be assumed for comparisons between measured and simulated event distributions if one is not explicitly given. The event categories used when plotting simulation predictions are as follows:

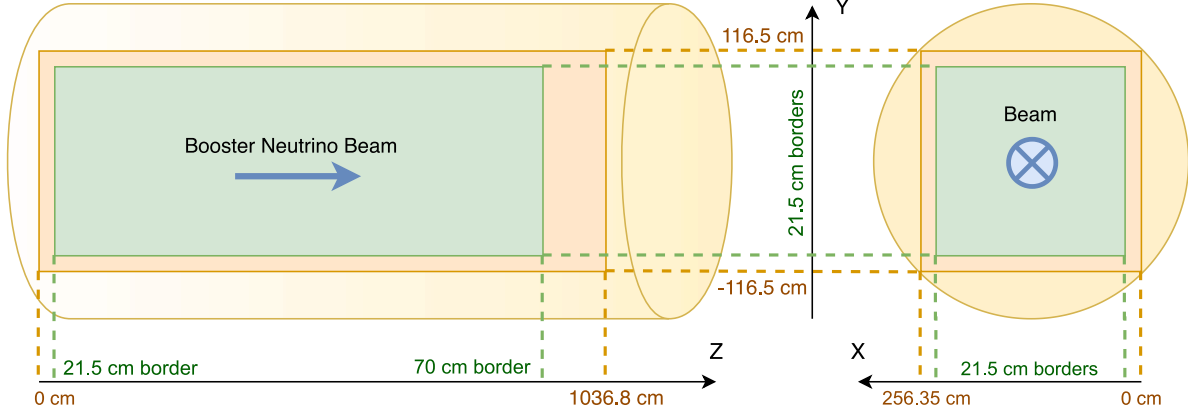[1]That is, the proton with the highest true momentum.

Figure 1: Fiducial volume adopted for this analysis. The yellow cylinder represents the MicroBooNE cryostat, the orange region represents the active volume of the TPC, and the green region is the fiducial volume. All dimensions are given in the standard detector coordinate system. The left (right) drawing shows a projection of the geometry on the YZ (XY) plane. This figure is adapted from a similar one found in Ref. [13].

Signal All events that satisfy signal requirement (1) through (6) from Section 3 (as determined by their MC truth information). These are divided into subcategories based on the true primary interaction. Signal events involving a primary interaction other than QE or 2p2h are placed into a catch-all "other" category. This category is dominated by resonant pion production followed by intranuclear absorption.

Out FV Events in which the true neutrino vertex falls outside of the fiducial volume defined in Section 3.1. These fail to satisfy signal requirement (1).

CC$N\pi$ Events containing a charged-current ν_μ interaction which produces one or more final-state pions. These fail to satisfy signal requirement (6). Note that ν_μ CC events containing final-state mesons other than pions fall into the next event category.

Other ν_μ CC Charged-current ν_μ events which do not fall into any of the previous categories. Among these are events which would otherwise be signal but do not satisfy the phase-space limits imposed by signal requirements (4) and (5). A small number of events containing final-state mesons other than pions are also present.

ν_e CC Events involving a charged-current ν_e interaction inside the fiducial volume. These fail to satisfy signal requirement (2).

NC Events in which a neutrino or antineutrino of any flavor undergoes a neutral-current interaction within the fiducial volume. These fail to satisfy signal requirement (2).

Beam-off Events from the beam-off data samples described in Section 2. These do not contain any simulated neutrino interactions and are used to estimate constant-in-time backgrounds.

Other All events which do not fall into one of the other categories defined above. These involve charged-current interactions of antineutrinos within the fiducial volume and thus fail to satisfy signal requirement (2).
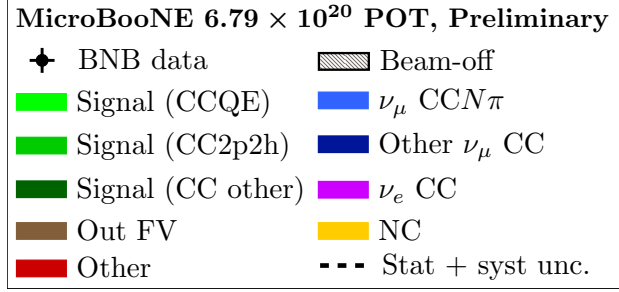
Figure 2: An example legend used in plots of event distributions in this note. The various event categories shown are defined in the text.

4 Event selection

The event selection adopted for this analysis is based on automated reconstruction tools developed within the Pandora framework [14]. Previous work from two related MicroBooNE efforts was used to guide the choice of specific analysis cuts. The preselection designed to identify inclusive charged-current ν_μ events is largely taken from studies presented by Wouter Van De Pontseele in his PhD thesis [13]. The additional cuts adopted to select mesonless final-states containing one or more protons are similar to those used in the original MicroBooNE CC$0\pi Np$ analysis [3].

4.1 CC inclusive preselection

In order of application, the selection criteria used to identify ν_μ CC candidate events are as follows:

(I) Neutrino identification: The event must pass the automated, Pandora-based *NeutrinoID* criteria documented in Ref. [13]. These criteria combine information from the time projection chamber (TPC) and photon detection system to perform a generic selection for neutrino interaction events and reduce the cosmic background in the selected sample.

(II) Fiducial volume: After correcting for space-charge effects [15], the reconstructed neutrino vertex must lie within the fiducial volume defined in Section 3.1.

(III) Contained starting points: The starting points for all reconstructed final-state primary particle candidates must lie within the containment volume defined in Section 4.2. The primary particle candidates are those which the Pandora-based reconstruction algorithms label as being direct daughters of the neutrino interaction (as opposed to, e.g., muon decay products).

(IV) Topological score: The *topological score* assigned to the event must be greater than 0.1. This variable represents the output of a support-vector machine designed to classify events as either neutrino-like (scores near 1) or cosmic-like (scores near 0). Further details are described in Ref. [13]. Figure 3 shows the measured distribution of this variable compared to the MicroBooNE MC prediction. The dashed lines show the boundaries of the one-sigma uncertainty band which includes all statistical and systematic contributions from MC events and measured beam-off background. This same uncertainty band is also represented by the shaded gray region in the ratio plot that appears below the main plot. A cut of topological score > 0.1 is sufficient to remove a large fraction of beam-off and out-of-fiducial-volume backgrounds.

(V) Muon identification: The event must contain a *muon candidate*, i.e., a reconstructed primary particle candidate that satisfies the following criteria:

(a) Track score: The *track score* assigned to the particle candidate must be greater than 0.8. This variable classifies reconstructed particles as shower-like (scores near 0, typical of electrons and photons) or track-like (scores near 1, typical of muons and protons). This is a loose cut that slightly increases the muon purity (see Fig. 4) by rejecting photons and shower-like cosmic activity.
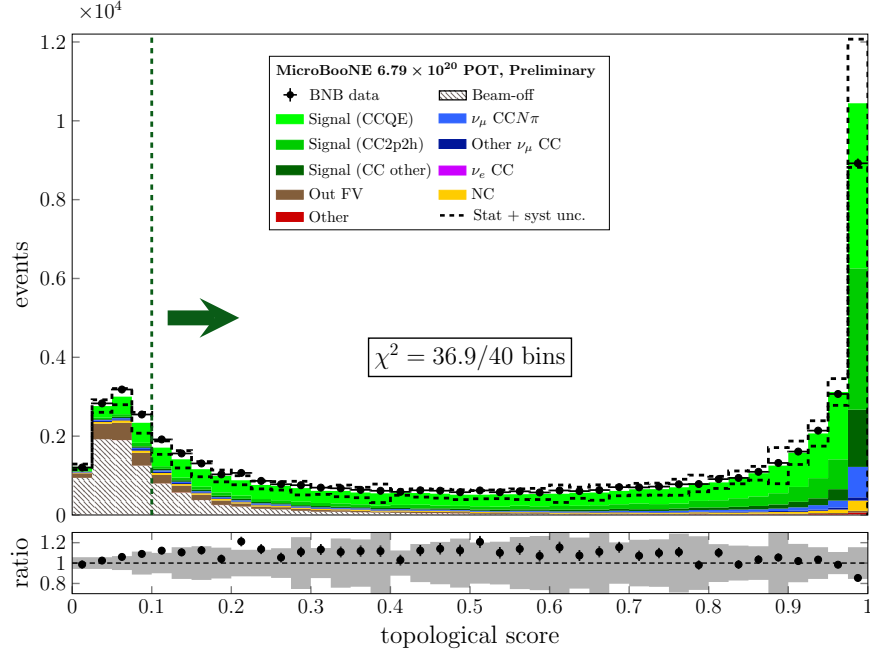
Figure 3: Topological score distribution for the full Runs 1–3 dataset. The portion near zero is dominated by beam-off events as expected. A cut of topological score > 0.1 is applied to reduce beam-off and out-of-fiducial-volume backgrounds. The green arrow points into the region in which events are accepted.
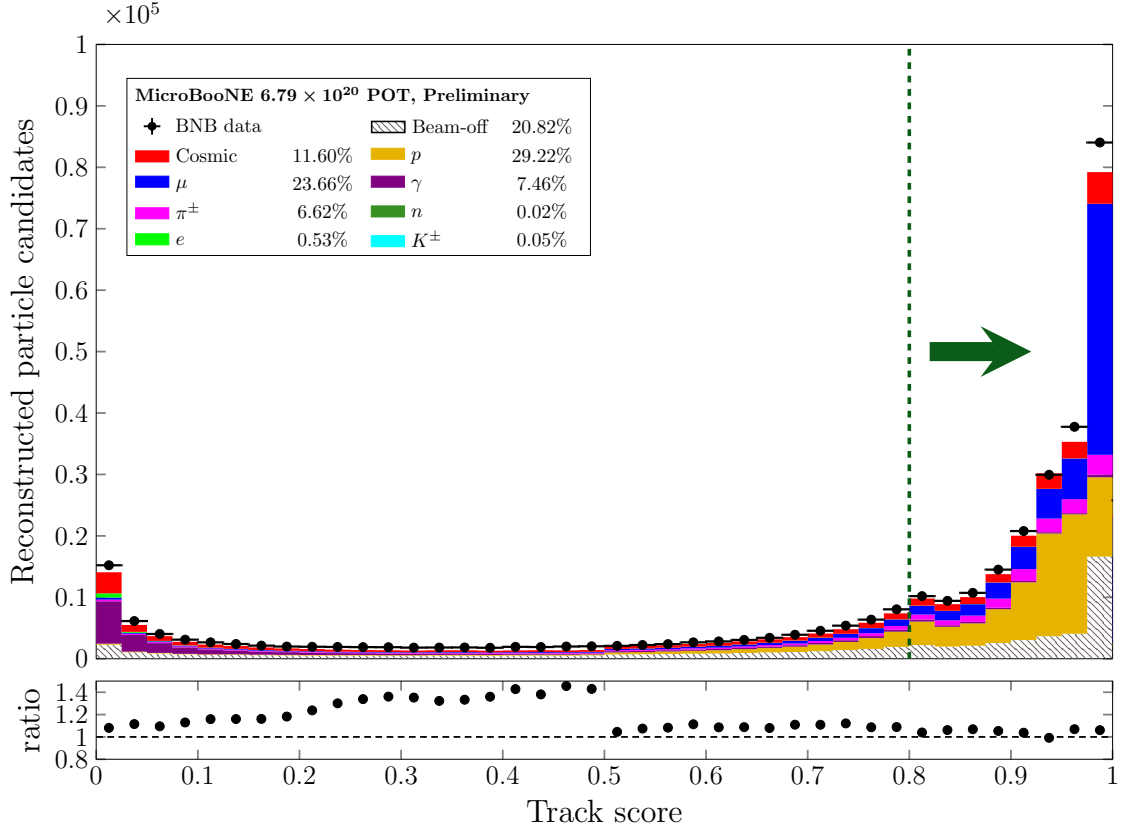

Figure 4: Track score cut applied to all reconstructed primary particle candidates when searching for a muon candidate. The green arrow points into the region in which particle candidates are accepted.
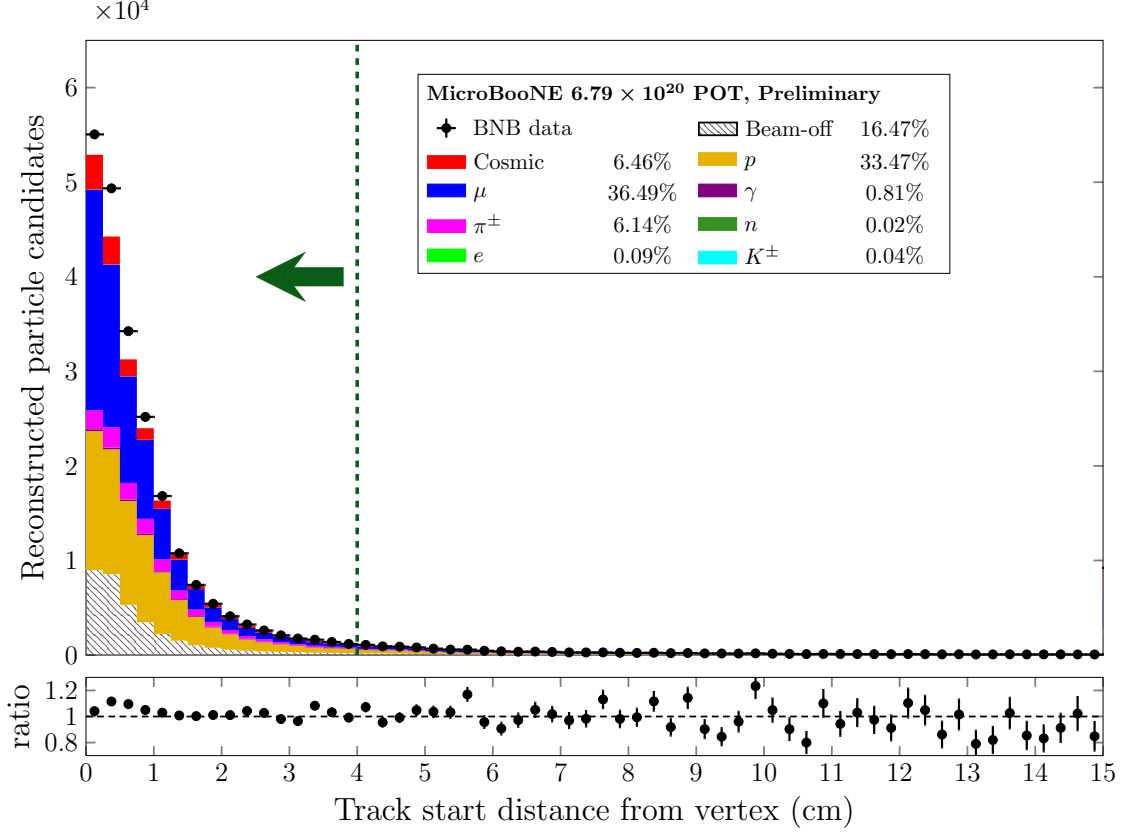
Figure 5: Cut applied to the distance between the reconstructed neutrino vertex and the muon candidate track. The green arrow points into the region in which particle candidates are accepted.

(b) Track start distance: The Euclidean distance between the track starting position and the reconstructed neutrino vertex position is less than 4 cm. This is a minor quality cut that helps to ensure that the muon candidate track is correctly associated with the reconstructed neutrino vertex (see Fig. 5).

(c) Track length: The length of the track is greater than 10 cm, which corresponds to a muon momentum of about 0.11 GeV/c. Tracks below this length are overwhelmingly generated by protons and cosmic activity (see Fig. 6). The muon threshold applied in signal requirement (4) helps to mitigate the impact of this cut on the efficiency for very low-energy muons.

(d) Muon particle ID: The log-likelihood ratio particle identification (LLR PID) score [16] is greater than 0.2. This variable is calculated by comparing track hit information from all three TPC wire planes to theoretical templates for muons and protons. The logarithm of a likelihood ratio for these two particle identification hypotheses is then converted to a score where -1 is most proton-like and 1 is most muon-like. The adopted cut value of 0.2 for the muon candidate is loose but does not significantly improve the product of efficiency times purity if it is moved closer to unity (see Fig. 7).

If two or more reconstructed primary particle candidates satisfy these criteria, the one with the highest LLR PID score (most muon-like) is considered the muon candidate.
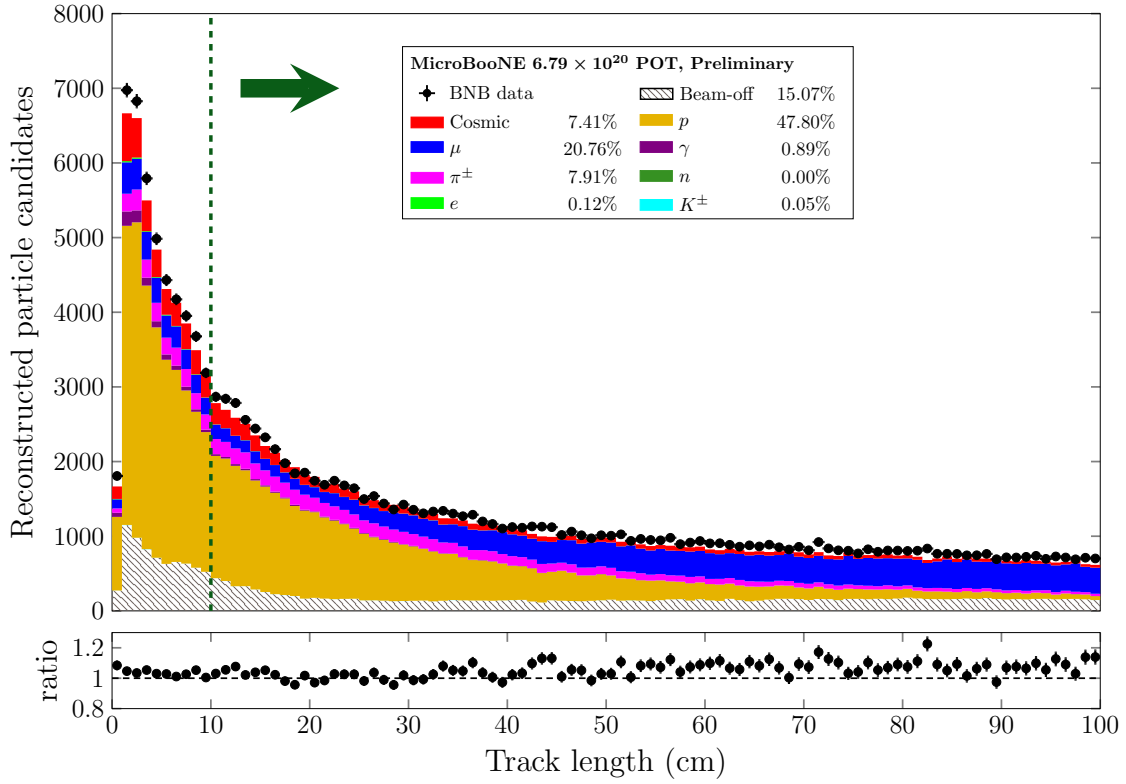
Figure 6: Track length cut applied to reconstructed particles when searching for a muon candidate. The green arrow points into the region in which reconstructed particles are accepted.
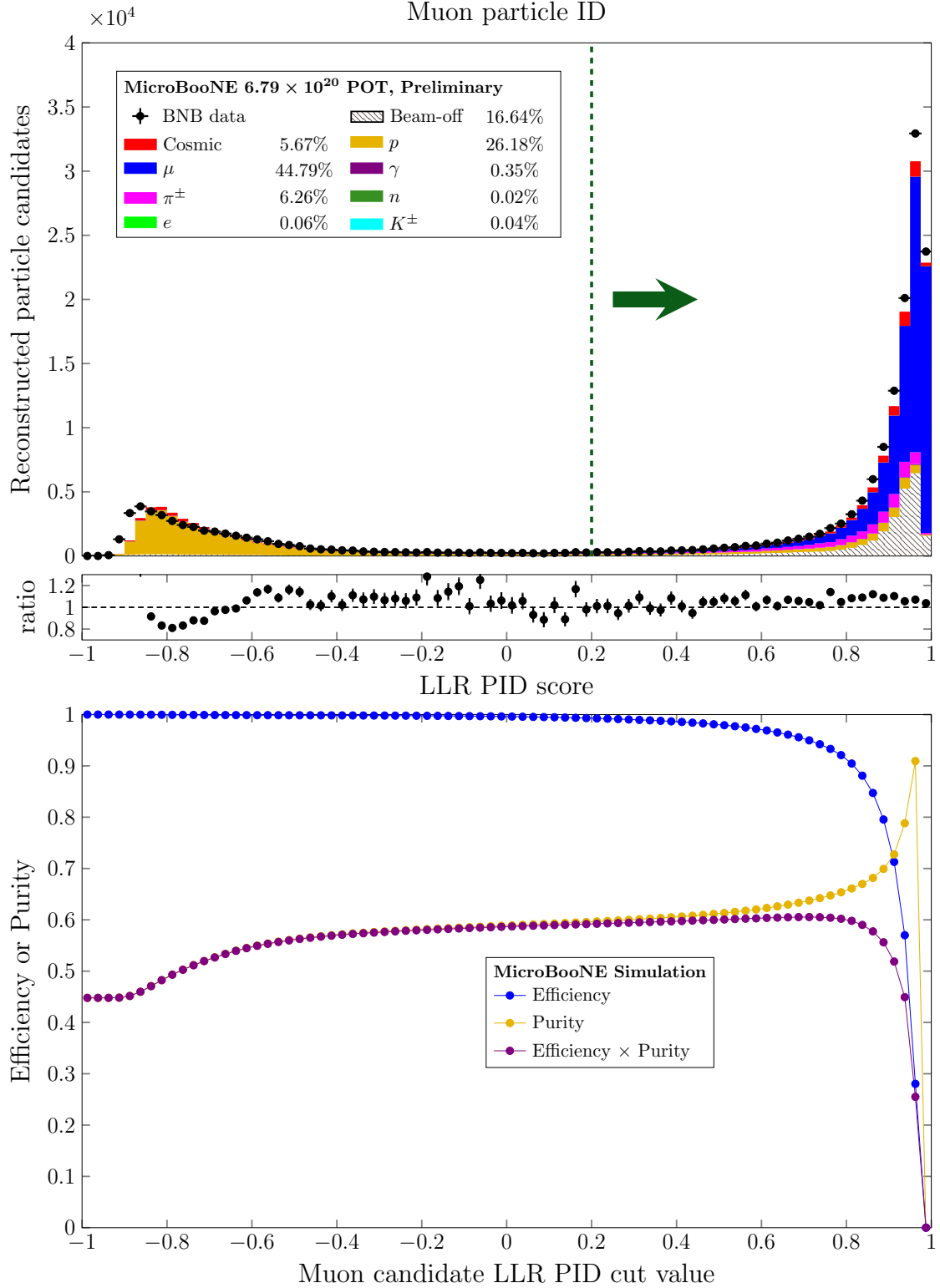
Figure 7: Log-likelihood ratio particle ID (LLR PID) cut applied to reconstructed particles when searching for a muon candidate. The upper plot shows the LLR PID score distribution. The cut value is given by the dashed green line, and muon candidates are accepted in the direction of the green arrow. The lower plot shows the running values of the efficiency (blue), purity (yellow), and the product of the two (purple) as a function of cut value.

4.2 Containment volume

As a quality cut to help ensure good reconstruction of particle momenta, all primary particles reconstructed by Pandora are required to start within a *containment volume* defined by

$$10 \text{ cm} < x < 246.35 \text{ cm}$$
$$-106.50 \text{ cm} < y < 106.50 \text{ cm}$$
$$10 \text{ cm} < z < 1026.80 \text{ cm}.$$

Apart from the muon candidate, all other primary particle candidates are also required to have end points within this same containment volume. The boundaries are chosen to provide a border of 10 cm between the containment volume and the edges of the TPC active volume in all directions. As explained in the next section, although the end point of the muon candidate track is not required to lie within the containment volume, the technique used to estimate the muon momentum depends on whether the end point is contained or not.

4.3 CC0πNp selection

To further isolate CC0πNp events, several cuts are applied that go beyond the CC inclusive preselection requirements described in Section 4.1. In order of application, these are

(VI) Zero showers: All reconstructed primary particle candidates must have a track score greater than 0.5 (ensuring that they are classified as more track-like than shower-like).

(VII) Multiple tracks: At least one such track that is not the muon candidate must be present in the event. All tracks that are not the muon candidate are considered proton candidates.

(VIII) Contained protons: All proton candidates must have reconstructed track end points that lie within the containment volume defined in Section 4.2. This is a quality cut intended to ensure that a range-based calculation of the proton momenta will be valid. No containment requirement is imposed on the muon candidate.

(IX) Proton particle ID: All proton candidates must have an LLR PID score less than 0.2. The chosen cut value 0.2 comes close to optimizing the product of efficiency and purity (see Fig. 8). Because low-momentum protons tend to cluster near LLR PID values of zero (see Fig. 10), the cut value was chosen high enough to allow for good acceptance across the full momentum range of interest.

A final set of two cuts is designed to ensure that the reconstructed particle momenta match the phase-space limits given in the signal definition:

(X) Muon threshold: The reconstructed muon momentum must be larger than 0.10 GeV/c. If the reconstructed end point of the muon candidate track is within the containment volume defined in Section 4.2, then a range-based estimate of its momentum is used. Otherwise, an estimate based on multiple Coulomb scattering (MCS) is used [17].

(XI) Proton momentum limits: The leading proton candidate, i.e., the proton candidate with the largest range-based reconstructed momentum p_p^{reco}, must satisfy the requirement 0.25 GeV/$c \leq p_p^{\text{reco}} \leq$ 1.20 GeV/c.

Events that satisfy all 11 selection criteria described above and in Section 4.1 are considered the CC0πNp candidates of interest for this analysis.

4.4 Choice of phase-space limits

Requirements (4) and (5) from the signal definition defined in Section 3 impose limits on the true momenta of the final-state muon and leading proton. Selection criteria (X) and (XI) impose identical limits on the reconstructed values of these quantities. The adopted muon threshold of 0.10 GeV/c is preserved unaltered from the previous MicroBooNE CC0πNp analysis [3]. It is motivated based on the minimum track length
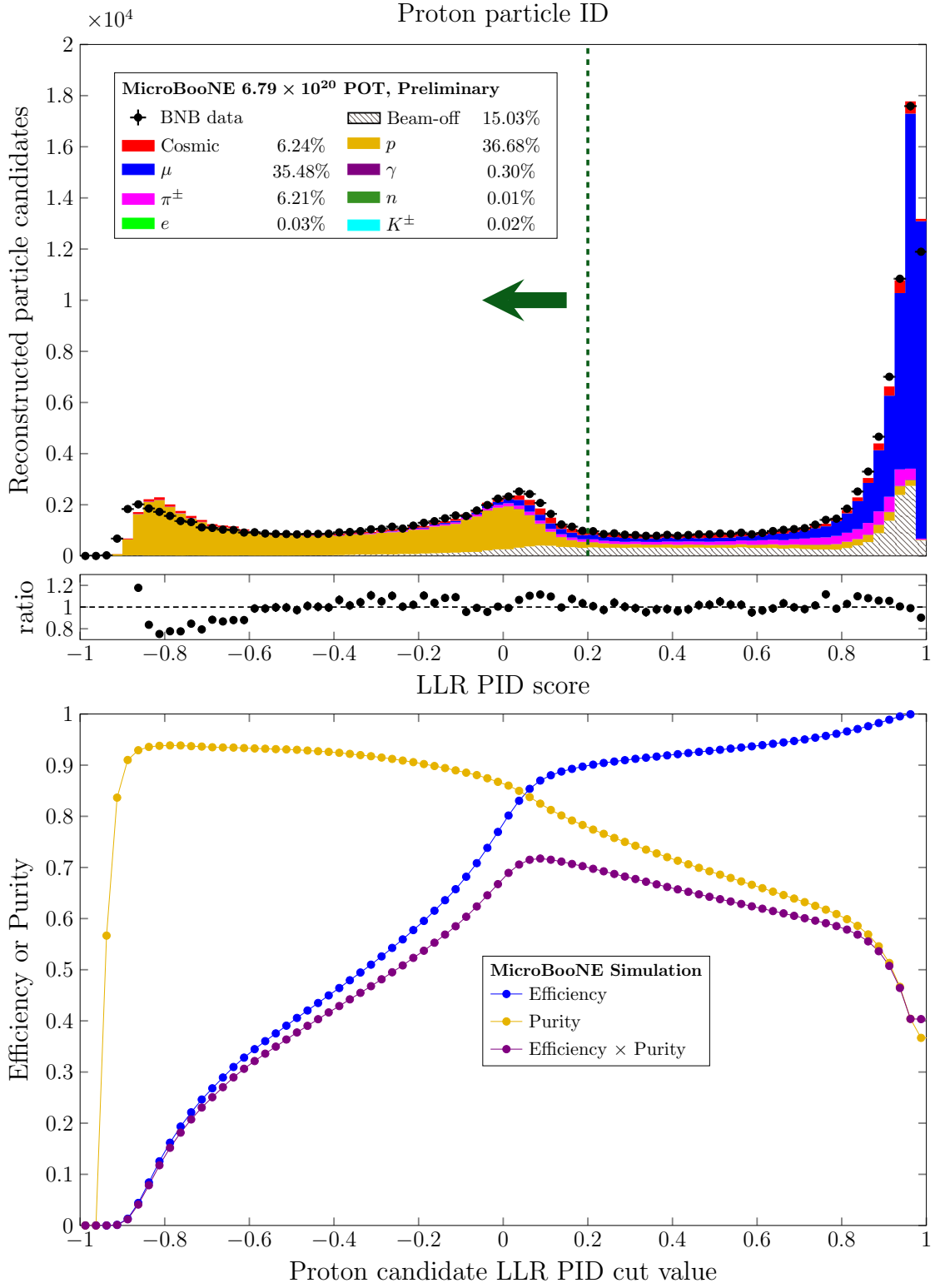
Figure 8: Log-likelihood ratio particle ID cut applied to proton candidate tracks. The same plotting conventions from Fig. 7 are used. Note that an LLR PID score near -1 is proton-like.
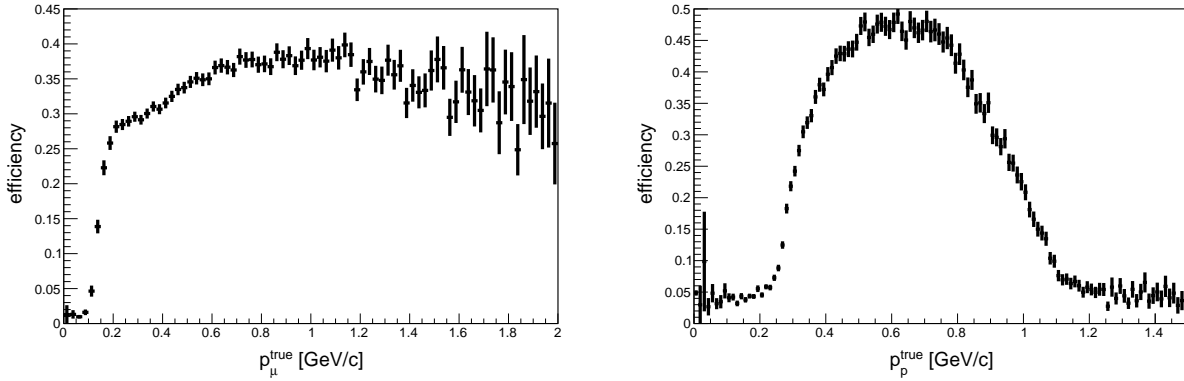
Figure 9: Selection efficiency as a function of the muon (left) and leading proton (right) true momentum. All signal and selection requirements are applied except for phase-space limits on these two momenta. Only MC statistical uncertainties are shown.

requirement of 10 cm for selecting the muon candidate, and it corresponds roughly to the muon threshold at which the selection efficiency begins to become appreciable (see the left-hand panel of Fig. 9).

The momentum threshold for the leading proton is of particular interest because theoretical modeling of neutrino-induced emission of low-energy nucleons is complicated and still poorly constrained by existing datasets. The previous $CC0\pi Np$ analysis adopted a value of 0.30 GeV/c. Thanks to a more sophisticated particle identification technique which makes use of information from all three TPC wire planes (see Sections 4.1 and 4.3), this analysis achieves a higher efficiency for low-momentum protons. As a consequence, the leading proton momentum threshold has been lowered to 0.25 GeV/c. The right-hand panel of Fig. 9 shows the selection efficiency as a function of true momentum of the leading proton in $CC0\pi Np$ events. The efficiency calculation is performed using all signal and event selection criteria described in this note except for the phase-space limits on the muon and leading proton. Although substantially smaller than the efficiency at 0.30 GeV/c, the efficiency at the chosen proton threshold of 0.25 GeV/c for this analysis is still appreciable and comparable to that near the upper momentum limit of 1.20 GeV/c, which was kept unaltered from the previous analysis [3]. The efficiency plateau seen in the right-hand plot in Fig. 9 may be attributed to two effects. Low-momentum protons (around 0.25 GeV/c) provide few TPC wire hits and are thus difficult to reconstruct successfully. High-momentum protons (around 1 GeV/c), on the other hand, are difficult to identify reliably using the current particle ID technique. Figure 10 shows the joint distribution of true momenta and LLR PID scores for all simulated protons in the CV MC sample which were successfully reconstructed. High-momentum protons tend to receive muon-like particle ID scores of around 0.6 or above and thus commonly fail selection requirement (IX). For neutrino interactions occurring near the edges of the fiducial volume, these protons also often exit the containment volume and thus fail to satisfy selection requirement (VIII).

Another key consideration in choosing the threshold for low-momentum protons is the expected quality of the momentum reconstruction. Figure 11 considers the bias in the reconstruction of low-momentum protons by plotting the distribution of the difference between the reconstructed and true momenta of the leading proton in simulated $CC0\pi Np$ events. As in Fig. 9, all signal and selection criteria are applied with the exception of the momentum requirements on the final-state muon and leading proton. Three true momentum bins are considered in the plot. The black histogram shows the probability distribution for protons just above the prior $CC0\pi Np$ analysis threshold of 0.30 GeV/c, while the blue and red histograms show lower-momentum protons in the next two decreasing increments of 0.05 GeV/c. The bias seen in the blue histogram for protons between 0.25–0.30 GeV/c is only modestly worse than that seen in the black histogram, with the two distributions having mean biases of 0.02 GeV/c and -0.01 GeV/c, respectively. However, the protons in the red histogram, which includes momenta between 0.20–0.25 GeV/c, are reconstructed far more poorly, with a mean bias of 0.11 GeV/c.
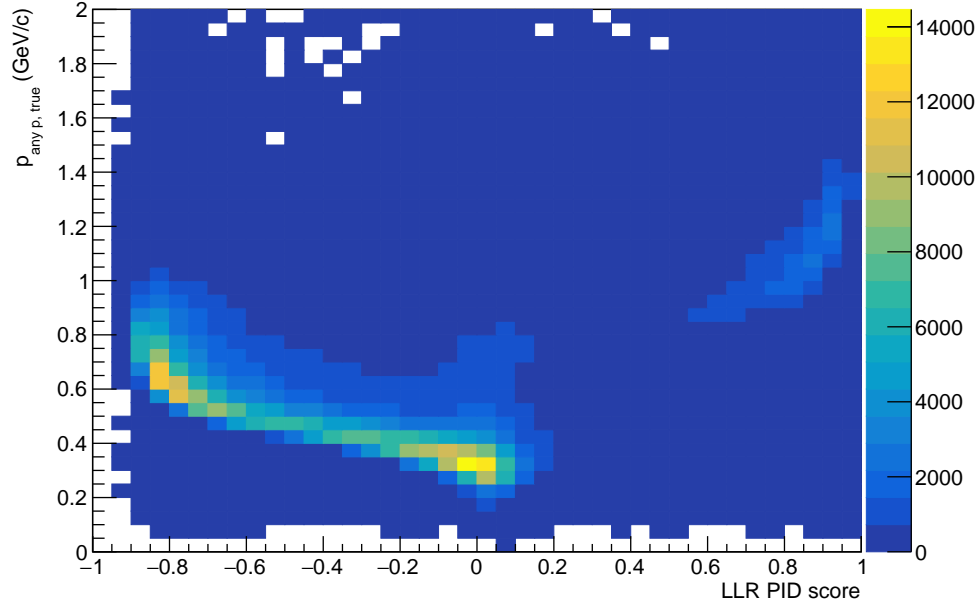
Figure 10: Joint distribution of true proton momentum and LLR particle ID score for all reconstructed protons in the MicroBooNE CV MC samples. Above about 1 GeV/c, the typical proton track begins to be classified as muon-like (LLR PID score $\gtrsim 0.6$).
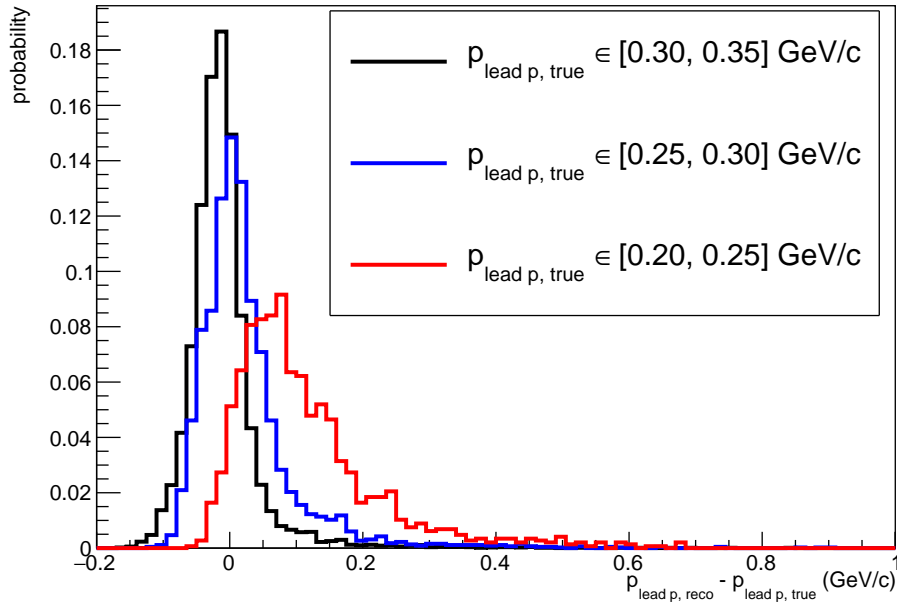

Figure 11: Bias distributions for reconstruction of the leading proton momentum in selected signal CC0πNp events. All signal and selection criteria are applied except for the muon and proton momentum limits.

4.5 Overall selection performance

Figure 12 shows three performance metrics for the selection cuts described in the previous subsections. All are calculated using the MicroBooNE central-value MC simulation. The efficiency ϵ is defined by the ratio

$$\epsilon \equiv \frac{N_{\mathrm{sel,sig}}}{N_{\mathrm{gen,sig}}} \tag{3}$$

where $N_{\mathrm{sel,sig}}$ is the number of selected signal events and $N_{\mathrm{gen,sig}}$ is the number of generated signal events present in the MC samples. The purity p is defined by

$$p \equiv \frac{N_{\mathrm{sel,sig}}}{N_{\mathrm{sel}}} \tag{4}$$

where N_{sel} is the total number of selected events, including simulated backgrounds and measured beam-off data. Since the latter can be used to subtract out the constant-in-time background contribution with only a small statistical uncertainty, it may also be useful to consider the "MC purity"

$$p_{\mathrm{MC}} \equiv \frac{N_{\mathrm{sel,sig}}}{N_{\mathrm{sel,MC}}} \,, \tag{5}$$

where $N_{\mathrm{sel,MC}}$ is the total number of selected events excluding those from the beam-off data sample.

The final CC0πNp selection used in this analysis achieves an overall efficiency of 36.6%, a purity of 77.4%, and an MC purity of 84.0%.
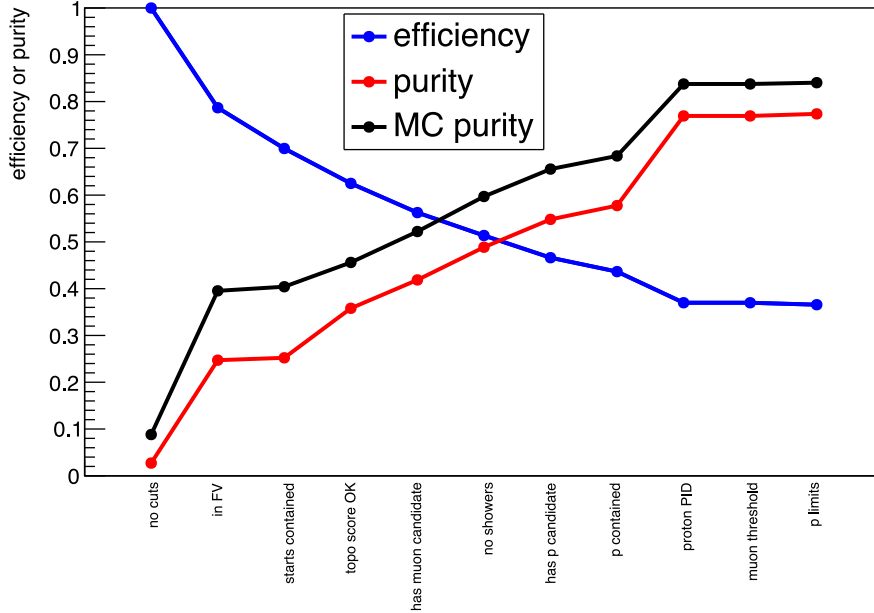
Figure 12: Evolution of the selection efficiency, purity, and MC purity as the various cuts described in the text are applied.

5 Bin definitions

A binning scheme was selected for the two double-differential measurements reported in this note by studying the expected signal event rates and detector resolution using the central-value MC simulation results. Variations of the bin edge definitions were performed "by hand" until a roughly optimal compromise was

achieved between very fine binning and two constraints: (1) a majority of selected events are reconstructed in the correct or the immediately adjacent two-dimensional bins, and (2) the expected signal events in each reconstructed bin are sufficient to mitigate the effect of MC statistical fluctuations on the evaluation of systematic uncertainties.

The effect of finite detector resolution on the reconstructed kinematic distributions may be quantified by a *migration matrix M*. Each element of this matrix M_{ij} represents a bin *occupancy*, i.e., the probability that a selected signal event generated in true bin j will be assigned to reconstructed bin i. This probability may be estimated from the MC simulation results via the expression

$$M_{ij} = \frac{\mu_{ij}}{\sum_i \mu_{ij}}, \tag{6}$$

where μ_{ij} is the number of simulated signal events which simultaneously belong to reconstructed bin i and true bin j. Identical bin definitions are used in true and reconstructed space for simplicity.

Figure 13 shows the migration matrix for the final choice of 2D bins adopted for the double-differential measurement of muon momentum and scattering cosine. Figure 14 shows the migration matrix obtained for the corresponding measurement of the leading proton. A reasonably diagonal migration matrix is achieved in both cases, with most events being reconstructed correctly or in the immediately adjacent bins of reconstructed momentum and angle. The main areas with relatively poor reconstruction are at low proton momentum, where angular resolution is limited, and in the overflow bin for muon momentum, for which a large majority of events are misreconstructed.

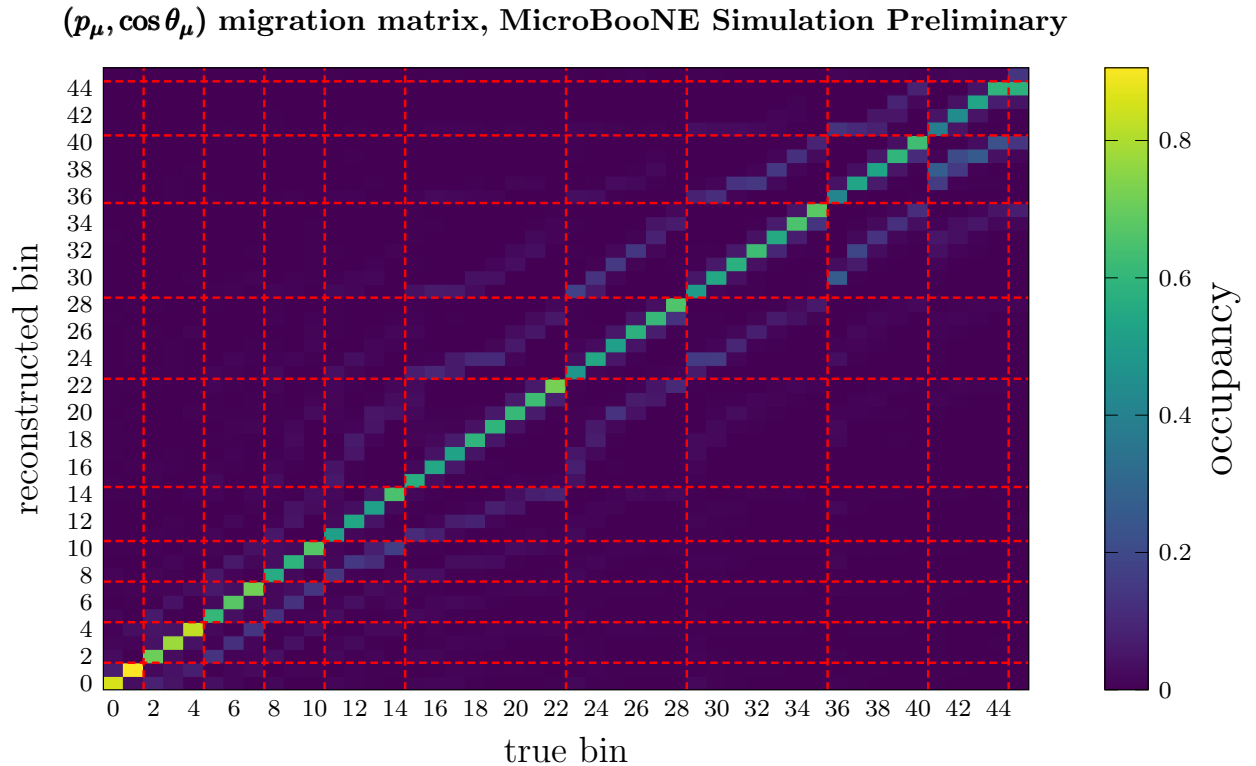**$(p_\mu, \cos\theta_\mu)$ migration matrix, MicroBooNE Simulation Preliminary**

Figure 13: Migration matrix for the chosen set of two-dimensional $(p_\mu, \cos\theta_\mu)$ bins. Dashed red lines indicate momentum bin boundaries. The features on either side of the diagonal represent smearing into incorrect reconstructed momentum bins.

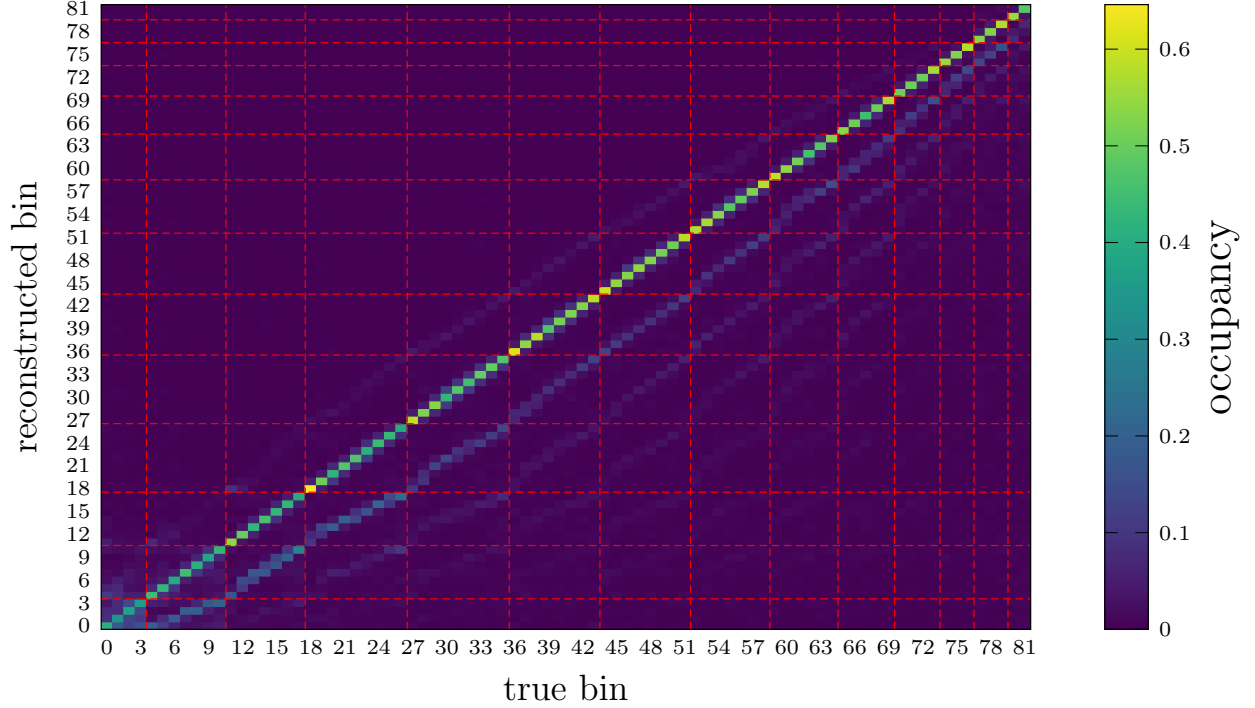**(p_p, cos θ_p)** migration matrix, MicroBooNE Simulation Preliminary

Figure 14: Migration matrix for the chosen set of two-dimensional $(p_p, \cos\theta_p)$ bins. Dashed red lines indicate momentum bin boundaries. The features on either side of the diagonal represent smearing into incorrect reconstructed momentum bins.

6   Systematic uncertainties

For the results presented in this note, systematic uncertainties are assessed on the expected number of selected events ν_i in each reconstructed bin i. The expected event count includes contributions from both simulated neutrino interactions and measured constant-in-time backgrounds. The uncertainty calculations rely on the observation that ν_i may be expressed in the form

$$\nu_i = \sum_j \Delta_{ij}\, \mu_j^{\text{CV}} + O_i + B_i \tag{7}$$

where μ_j^{CV} is the expected number of signal CC0πNp events in true bin j and O_i (B_i) is the number of measured beam-off background events (simulated beam-correlated background events) in reconstructed bin i. All three of these quantities are pre-scaled according to the procedure described in Section 2 to match the total beam exposure used for the measurements. The event counts obtained from Monte Carlo simulations (μ_j^{CV} and B_i) are calculated using the event weights needed to apply the MicroBooNE GENIE tune [7]. The sum over j includes all true bins. These are chosen so that any event which satisfies the signal definition requirements will belong to a unique true bin.

The *response matrix* Δ_{ij} transforms a prediction of signal event counts in true bins j into a corresponding prediction in reconstructed bins i. It accounts for both inefficiency and bin migration effects introduced by imperfect event reconstruction in the detector. Each element of the response matrix is estimated from the MC simulation results according to the relation

$$\Delta_{ij} \equiv \frac{\mu_{ij}}{\mu_j^{\phi_{\text{CV}}}}, \tag{8}$$

where μ_{ij} is the number of signal events which fall simultaneously into true bin j and reconstructed bin i. The quantity $\mu_j^{\phi_{\text{CV}}}$ is the number of signal events in true bin j. The superscript $^{\phi_{\text{CV}}}$ indicates that this

quantity should always be evaluated using the central-value estimate of the incident neutrino flux, regardless of any flux variations which may need to be applied to μ_{ij} in the numerator of Δ_{ij}. Likewise, the superscript $^{\mathrm{CV}}$ used to label μ_j^{CV} in Eq. (7) indicates that the central-value signal event prediction should always be used regardless of any MC simulation model variations that may be applied elsewhere. The purpose of these special superscripts will be explained shortly.

Uncertainties are quantified in this analysis using covariance matrices calculated according to a multiple-universe procedure. Under this approach, the covariance between the predicted event counts ν_a and ν_b (which are calculated according to Eqs. (7) and (8)) in two reconstructed bins a and b is represented by the matrix element

$$V_{ab} = \frac{1}{N_{\mathrm{univ}}} \sum_{u=1}^{N_{\mathrm{univ}}} \left(\nu_a^{\mathrm{CV}} - \nu_a^u\right)\left(\nu_b^{\mathrm{CV}} - \nu_b^u\right). \tag{9}$$

Here ν_a^{CV} is the total event count in reconstructed bin a predicted by the central-value MC simulations. The variable ν_a^u is a prediction of the same quantity computed based on an alternate simulation (i.e., in an alternate *universe*) in which some aspect of the models used to describe the beam, particle interactions, or the detector response has been changed from the adopted central value. The number of alternate universes N_{univ} considered when evaluating the sum in Eq. (9) depends on the particular systematic uncertainty of interest. Covariance matrices V_{ab} are calculated individually for each source of uncertainty described in the following subsections. A total covariance matrix is then obtained by summing the individual matrices.

The use of the $^{\mathrm{CV}}$ and $^{\phi_{\mathrm{CV}}}$ superscripts in Eqs. (7) and (8) enables the treatment of systematic uncertainties presented here to match the one anticipated in a final extraction of double-differential cross sections. In the context of a cross-section measurement, systematic uncertainties affecting the expected number of selected signal events are normally relevant only through their effect on the efficiency and bin migration corrections applied via the response matrix. Therefore, when Eq. (7) is evaluated in each alternate universe, the response matrix elements Δ_{ij} are allowed to vary, but the signal event counts μ_j^{CV} in each true bin j are held fixed at the prediction obtained from the central-value MC simulation.

An exception to the usual procedure occurs for flux variations. For each alternate universe in which a modified model of the neutrino flux is used, the denominator of the response matrix element from Eq. (8) is equal to the central-value signal event count:

$$\mu_j^{\phi_{\mathrm{CV}}} = \mu_j^{\mathrm{CV}}. \tag{10}$$

In this case, Eq. (7) reduces to the expression

$$\nu_i = \mu_i + O_i + B_i \tag{11}$$

where

$$\mu_i = \sum_j \mu_{ij} \tag{12}$$

is the number of signal events in reconstructed bin i predicted using the alternate model of the neutrino flux. Thus, for flux systematic uncertainties, both signal (μ_i) and beam-correlated background (B_i) events are treated on an equal footing. Since the full uncertainty on the incident neutrino flux is already calculated in this way for both signal and beam-correlated background events, extraction of the final flux-averaged differential cross-section results may proceed using the *central-value* integrated flux. This approach may be contrasted with an attempt to extract a cross section in the (unknown) true neutrino flux [18].

The use of covariance matrices in this analysis implies that all uncertainties are assumed to follow a multivariate Gaussian distribution about the central value.

6.1 Neutrino interaction modeling

Theoretical uncertainties on MicroBooNE's neutrino interaction model are assessed using a framework provided by GENIE together with some MicroBooNE-specific additions [7]. To avoid the computationally intensive task of generating many MC samples using modified versions of the central-value interaction model, a reweighting strategy is adopted instead: each GENIE event present in the original MC samples is assigned a weight W^u in the alternate universe u defined by the likelihood ratio

$$W^u \equiv \frac{P^u}{P^{\mathrm{CV}}}. \tag{13}$$

Model variation	Universes	Interpretation
AxFFCCQEshape	1	Switch to the z-expansion axial form factor for CCQE, consider the shape-only effect on the cross-section
DecayAngMEC	1	Use a $\cos^2\theta$ angular distribution rather than an isotropic one for decaying the outgoing pre-FSI cluster of two nucleons in 2p2h events
NormCCCOH	1	Increase the CC coherent π production cross section by 100%
NormNCCOH	1	Increase the NC coherent π production cross section by 100%
RPA_CCQE	2	Vary the strength of RPA corrections for CCQE by $\pm 1\sigma$
ThetaDelta2NRad	1	Use a $\cos^2\theta$ angular distribution for the emitted photon rather than an isotropic one in radiative Δ baryon decays
Theta_Delta2Npi	1	Use an isotropic pion angular distribution rather than the Rein-Sehgal prediction in $\Delta \to N + \pi$ decays
VecFFCCQEshape	1	Switch to a dipole vector form factor for CCQE, consider the shape-only effect on the cross-section
XSecShape_CCMEC	1	Switch to the Valencia model prediction for the shape of the leptonic differential cross section in CC 2p2h events

Table 2: GENIE unisim variations considered when assessing neutrino cross-section model uncertainties

Here P^{CV} is the probability of generating the event according to the central-value GENIE interaction model and P^u is the corresponding probability for the varied model in alternate universe u.[2] The weights W^u are employed when calculating the alternate-universe event counts ν_a^u and ν_b^u that appear in Eq. (9).

The neutrino interaction uncertainties considered in this analysis may be grouped into three general categories.

GENIE unisim variations represent a change to one aspect of the cross-section model in isolation. Typically only a single alternate universe is constructed in which the change is applied. The sole exception is RPA_CCQE, the systematic uncertainty related to the strength of the Random Phase Approximation (RPA) corrections included in the GENIE CCQE model. For this uncertainty, two alternate universes are used which correspond to plus and minus one-sigma variations. Table 2 summarizes the GENIE unisim variations considered in the present analysis.

GENIE multisim alternate universes are produced by varying 44 model parameters simultaneously. The value of each parameter is randomly sampled about its central value from an independent Gaussian distribution with a width based on the parameter's one-sigma uncertainty. A set of $N_{\mathrm{univ}} = 600$ alternate universes is used to calculate the GENIE multisim covariance matrix.

Second-class current (SCC) variations account for possible small contributions to the CCQE cross section from two additional form factors ($F_3^V(Q^2)$ and $F_3^A(Q^2)$) which might be nonvanishing [19]. Ratios between a cross-section calculation with the NEUT [20] generator (which includes the SCC form factors) and one from GENIE (which does not) are used to obtain the needed event weights.

Further details about MicroBooNE's approach to systematic uncertainties related to neutrino interaction modeling are available in Ref. [7].

---

[2]Depending on the specific model variation considered, the variables P^{CV} and P^u may actually denote probability *densities* rather than probabilities. This distinction is ignored in the text since it is unnecessary for a conceptual understanding of the reweighting technique.

6.2 Neutrino flux

Systematic uncertainties related to the Booster Neutrino Beam flux are calculated using a reweighting strategy similar to the one described for the GENIE interaction model in the previous section. Alternate universes representing changes to the central-value flux model are formed using two categories of variations:

Beam unisims represent modifications to aspects of the beam simulation unrelated to modeling of hadron production in $p + $ Be collisions. These include the uncertainty on the horn current, on the magnitude of a *skin effect* related to the depth with which the current penetrates into the horn conductor, and on several pion-nucleus and nucleon-nucleus cross sections for aluminum and beryllium targets.

Hadron production model uncertainties are assessed separately for charged pions, positive kaons, negative kaons, and neutral kaons.

A single set of 1000 universes representing the combined effect of all flux variations is adopted for computing flux systematic uncertainties. Further documentation of MicroBooNE's BNB flux model and uncertainties is available in Ref. [8].

6.3 Reinteractions

Following the primary neutrino interaction, the outgoing particles that escape the struck nucleus may rescatter on other nuclei within the detector. The Geant4 [10] toolkit is used for modeling particle transport of this kind in MicroBooNE MC simulations. The Geant4Reweight [21] package is used to assess related systematic uncertainties. The present treatment of reinteraction uncertainties considers variations of the Geant4 total cross section model for positive pions, negative pions, and protons. For protons, variations are applied to the elastic and reaction (i.e., total inelastic) channels separately. For pions, the elastic, quasielastic, absorption, single charge-exchange, double charge-exchange, and pion production channels are individually varied. The size of the variations considered is typically on the order of 10%.

Like the flux variations discussed in the previous section, a single set of event weights for $N_{\mathrm{univ}} = 1000$ alternate universes is calculated. These represent the combined effect of all of the reinteraction cross-section model variations. They are used to calculate the elements of a single covariance matrix describing overall reinteraction uncertainties in the present analysis.

6.4 Detector response

In contrast to the uncertainties mentioned in the previous sections, detector systematic uncertainties are computed using dedicated *DetVar* MC samples (see Section 2) in which each alternate universe is explicitly simulated. Three categories of detector response model variations are considered:

Wire modification variations apply data-driven transformations to the simulated width and amplitude of deconvolved TPC wire waveforms. The transformations are a function of position and direction of flight for the particle of interest. Precalculated splines based on data/MC ratios observed in a sample of measured anode-cathode-piercing tracks (ACPT) are used to apply the transformations to the wire signals. Separate variations are simulated to account for the dependence of the needed transformations on x, y and z, θ_{xz}, and θ_{yz} in the detector coordinates. Further details about the wire modification approach to detector systematics are available in Ref. [22].

Light yield variations account for uncertainties that affect the response of the photomultiplier tubes. Three alternate universes are considered. The *Light Yield Down* universe reduces the overall light yield of energy depositions in the detector by 25%. The *Light Yield Attenuation* universe is similar but the correction is position-dependent. An absorption length of 10 m is used in the variation. The *Light Yield Rayleigh* universe increases the Rayleigh scattering length assumed in the detector simulation by 50%.

Other detector variations change aspects of the simulated TPC response to charged particles. The *Space Charge Effect* (SCE) universe applies distortions to the simulated electric field and ionization electron drift trajectories using an alternative model. The *Recombination 2* universe changes the values of the α and β parameters used in the modified box model [23] used to simulate ionization.

An individual covariance matrix is calculated for each detector variation universe in isolation. The sum of these covariance matrices quantifies the full systematic uncertainty related to mismodeling of the detector response. All universes for the wire modification and light yield variations are constructed using dedicated MC samples corresponding to a simulated beam exposure of 1.24×10^{21} POT. To minimize MC statistical fluctuations, these samples (collectively labeled *DetVar1* in Table 1) share the same input GENIE events and differ only in the downstream detector simulation. The two other variations are treated in a similar way, but the dedicated samples (labeled *DetVar2*) correspond to a smaller beam exposure of 6.13×10^{20} POT.

6.5 Beam exposure

The protons delivered to the Booster Neutrino Beam target are monitored using a set of two toroids. The uncertainty on the beam exposure (protons-on-target) reported by these toroids has been found to be 2% in routine calibrations [24]. This uncertainty is included in this analysis as a 2% normalization uncertainty on the beam-correlated event count in all reconstructed bins. In this case, the expression for the covariance matrix element from Eq. (7) reduces to

$$V_{ab} = (\nu_a^{\mathrm{CV}} - O_a)(\nu_b^{\mathrm{CV}} - O_b)f^2 \tag{14}$$

where $f = 0.02$ is the fractional uncertainty. The measured beam-off contribution is subtracted from each of the first two factors since it is unaffected by this systematic uncertainty.

6.6 Number of target nuclei

Based on a conservative estimate of the uncertainty associated with variations in the temperature and pressure of the liquid argon target, this analysis adopts a 1% fractional uncertainty on the number of argon nuclei present in the fiducial volume. The covariance matrix for this systematic uncertainty is calculated using a procedure identical to the one described in Section 6.5 except that, in this case, $f = 0.01$.

6.7 Statistical uncertainty on the prediction

Two kinds of statistical uncertainties are calculated on the predicted number of events in each bin. These are combined with the systematic uncertainties mentioned above to form the complete error envelope. The first statistical uncertainty arises due to the finite number of MC events included in the CV samples described in Section 2. The elements V_{ab} of the covariance matrix representing the MC statistical uncertainty are computed according to the relation

$$V_{ab} = \delta_{ab} \sum_{e=1}^{n_a} w_e^2 \tag{15}$$

where δ_{ab} is the Kronecker delta function, n_a is the number of simulated events (both signal and background) in the ath bin, and w_e is the weight of the eth of these events (taking into account both the reweighting needed to apply the MicroBooNE GENIE tune and the scaling factors needed to account for the relative normalizations of the various MC samples). Note that when $a \neq b$, the covariance matrix element V_{ab} vanishes. That is, the MC statistical uncertainties have zero bin-to-bin correlations.

The second statistical uncertainty on the prediction arises because of the finite number of measured beam-off background events. The covariance matrix representing this uncertainty is calculated using a similar procedure, except that the sum of squared MC event weights is replaced with O_a, the number of selected off-beam events found in the ath reco bin:

$$V_{ab} = \delta_{ab} S_{\mathrm{off}}^2 O_a . \tag{16}$$

The scale factor S_{off} renormalizes the beam-off event rate to the beam-on data as described in Section 2.

6.8 Impact on predicted event distributions

Figures 15 and 16 apply the procedures described in the preceding subsections to the calculation of fractional uncertainties in each reconstructed bin of interest for this analysis. A total uncertainty (solid black) is

shown in addition to the overall contributions from the major categories discussed above. Detector response uncertainties are often largest, but flux and cross-section uncertainties are higher in some bins. Reinteraction uncertainties are small across most of the phase space, but they play an important role at high proton momentum.
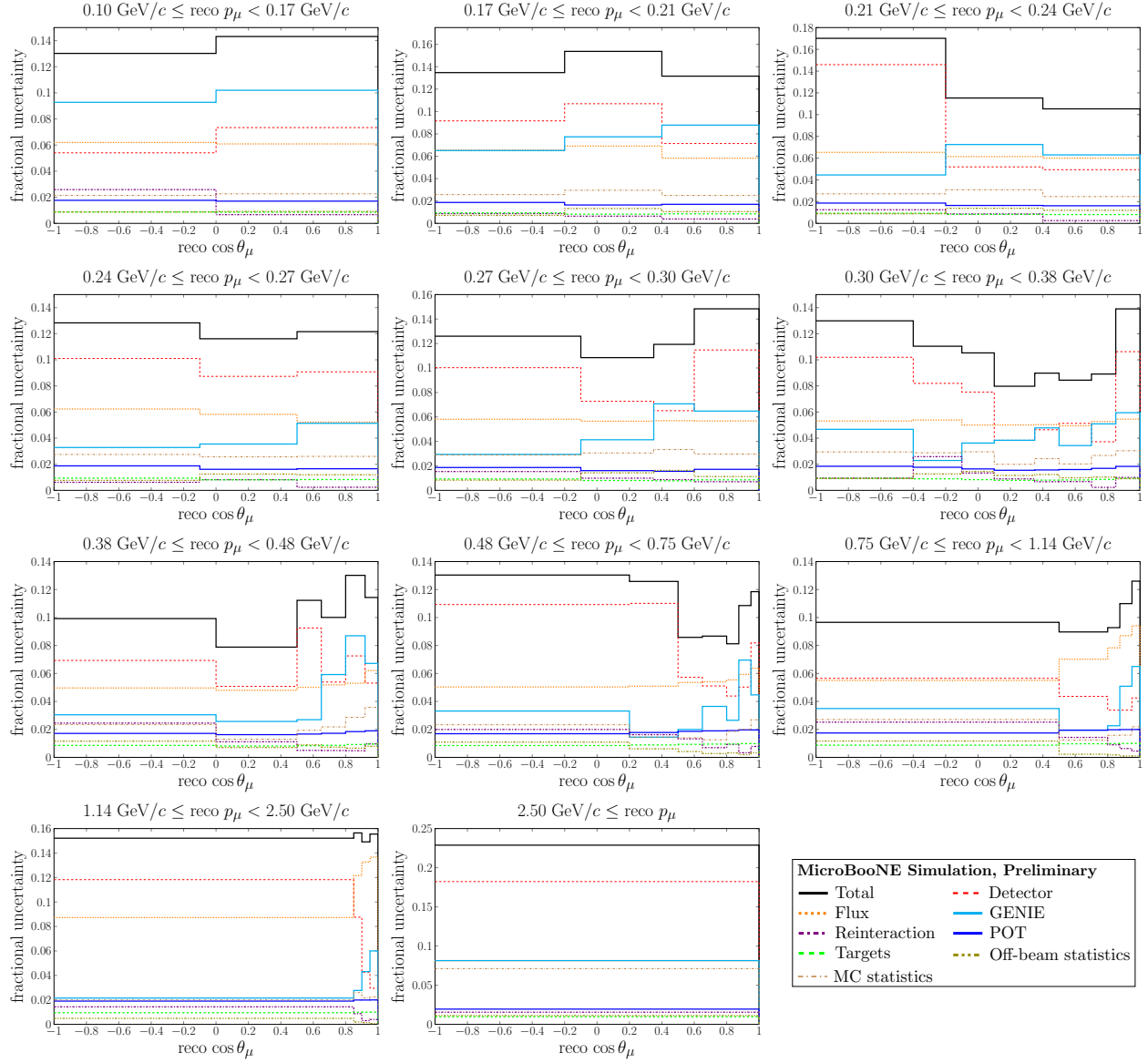
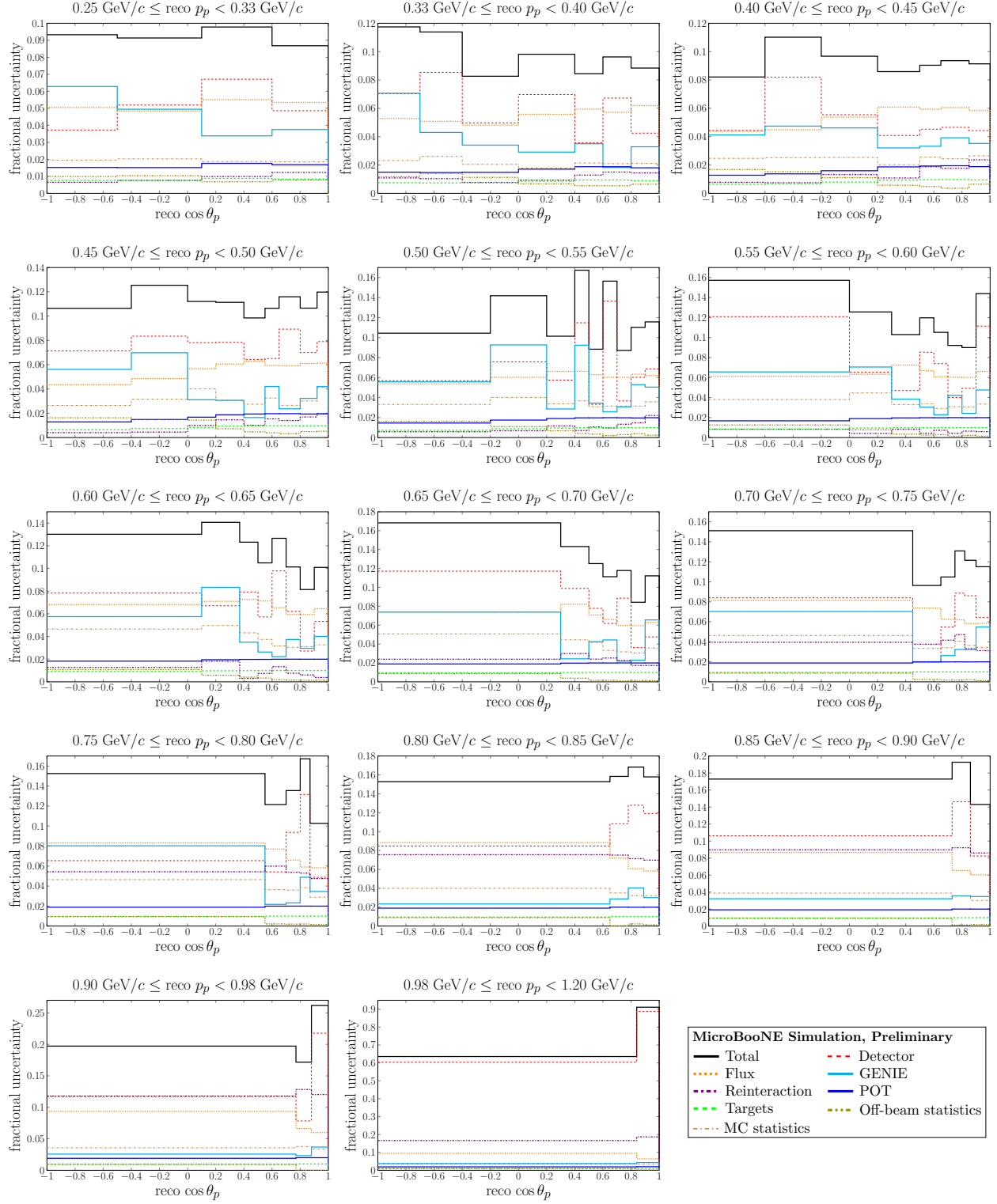Figure 15: Fractional uncertainties evaluated in each bin used for the $(p_\mu, \cos\theta_\mu)$ measurement

Figure 16: Fractional uncertainties evaluated in each bin used for the $(p_p, \cos\theta_p)$ measurement

7 Results

Figures 17 and 18 show the measured double-differential event distributions obtained using the procedures outlined in earlier sections of this note. Each panel displays the angular distribution within a particular momentum bin defined by the expression in the panel title. The color scheme used for the MicroBooNE MC predictions is the same as the one defined in Fig. 2. Uncertainties on the black points are purely from data statistics. The dashed black lines around the MC prediction denote the boundaries of the 1σ error band which includes all statistical and systematic uncertainties discussed in Section 6. Individual χ^2 values are given for each panel considered independently of all others. A total χ^2 value is also quoted near the legend at the bottom of each figure. This is calculated while accounting for correlations between all reconstructed bins using the full covariance matrix.

The double-differential event rate measurement for muon kinematics shows a dramatic deficit relative to the MicroBooNE MC prediction in the largest momentum bins. A noticeable excess is also present in some angular bins at momentum of a few hundred MeV/c. The proton angular distribution is typically well-described within individual momentum bins. The MC model has more difficulty in fully accounting for the bin-to-bin correlations observed in the full dataset, but the achieved χ^2 value of 126 for the 82-bin leading proton measurement is still considerably better than for the muon case ($\chi^2 = 334$ for 46 bins).

Figures 19 and 20 show the same distributions projected onto a single axis as a function of reconstructed bin number. These plots provide a compact means of viewing the results from the full measurement.

Figures 21 and 22 show the corresponding single-differential momentum distributions integrated over the full angular range. Good agreement is seen between the data and MC prediction at the lowest values of the muon momentum, although beam-correlated backgrounds are seen to be significant in that region. Noticeable tension is seen between the MC results and the data over the remainder of the momentum range. The model description of the leading proton momentum is noticeably better but leaves some room for improvement with a χ^2 value of 44.6 for 14 momentum bins. Notably, the MC prediction comes quite close to the data point in the lowest proton momentum bin, which probes a region 50 MeV/c lower than the previous MicroBooNE CC0πNp analysis [3].

Finally, Fig. 23 shows the measured CC0πNp event rate in a single bin which has been integrated over all momenta and scattering angles, including the overflow bin for muon momenta. Despite clear areas of tension in the differential distributions, the overall event rate is comfortably within the one-sigma uncertainties on the MC prediction.
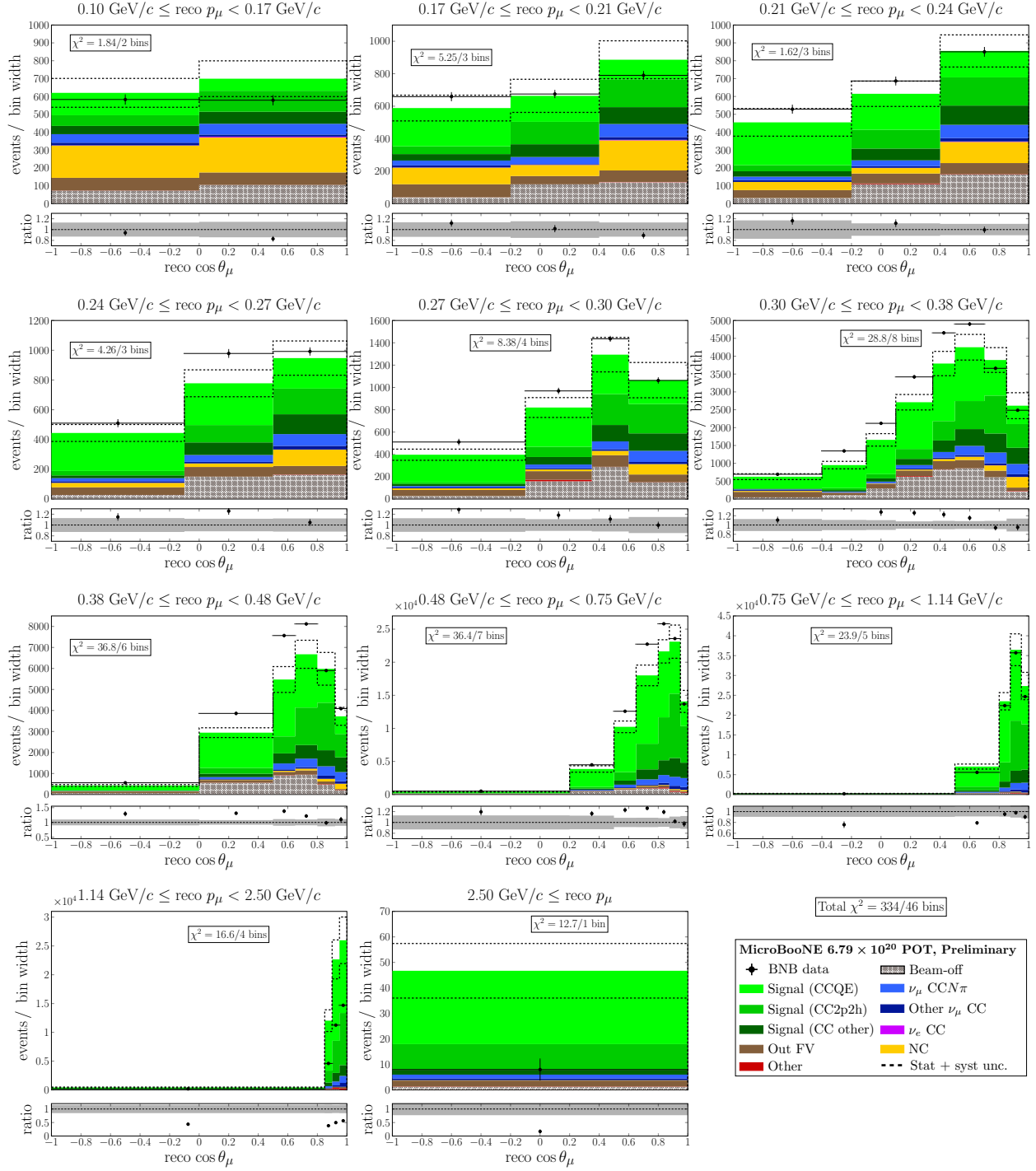
Figure 17: Comparison between the measured double-differential distribution of $(p_\mu, \cos\theta_\mu)$ and the event counts predicted by MicroBooNE MC simulations. The dashed lines show the full uncertainty (statistical plus systematic) on the MC prediction.
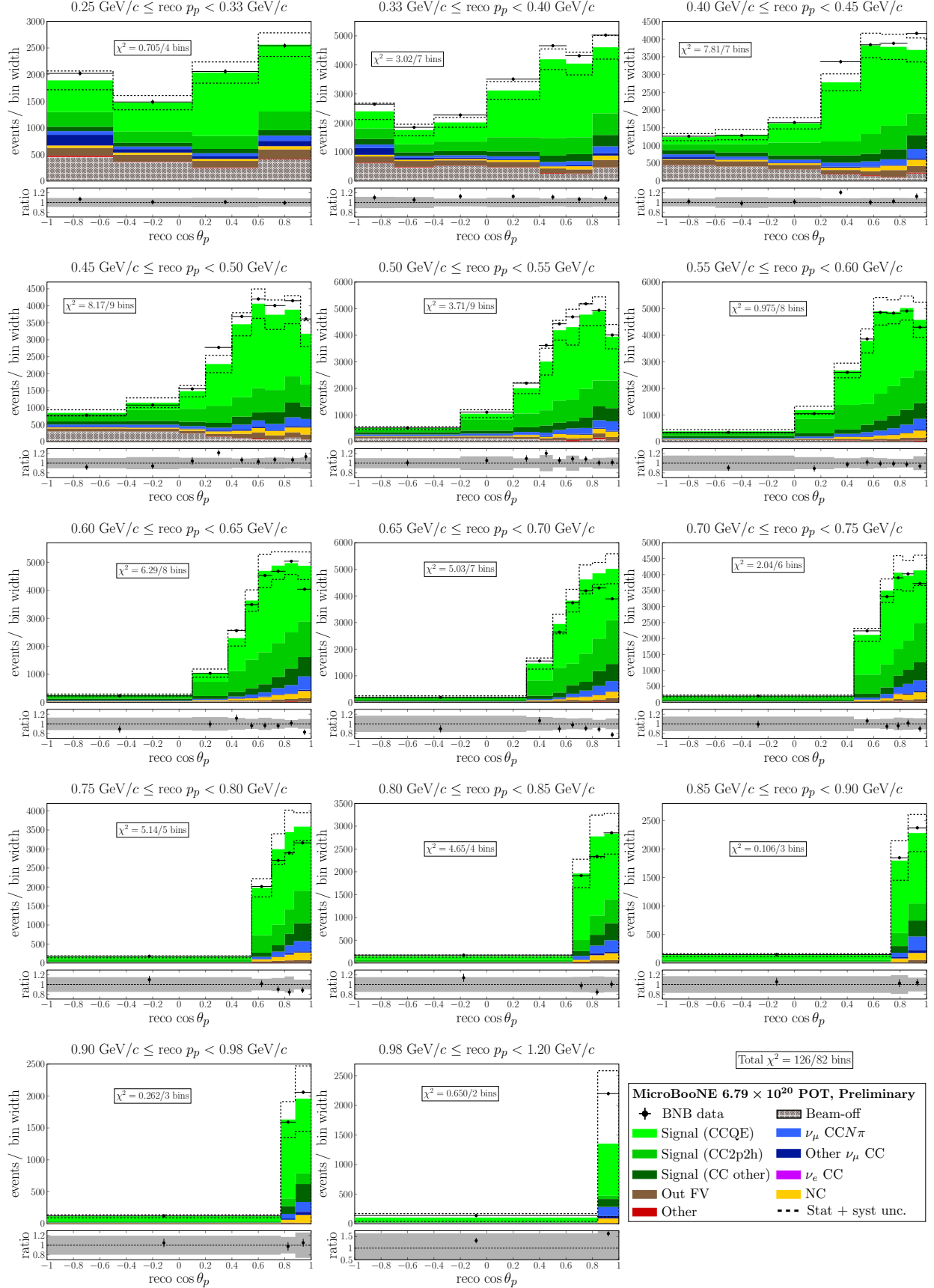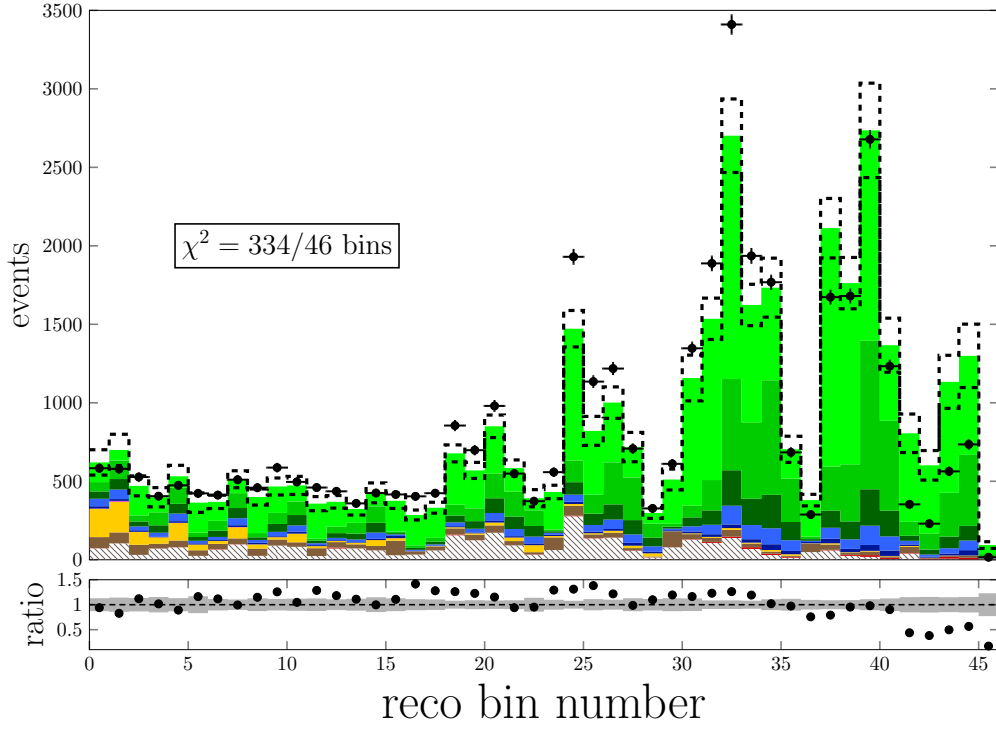
Figure 18: Comparison between the measured double-differential distribution of $(p_p, \cos\theta_p)$ and the event counts predicted by MicroBooNE MC simulations. The dashed lines show the full uncertainty (statistical plus systematic) on the MC prediction.

Figure 19: Summary plot for the full double-differential measurement of $(p_\mu, \cos\theta_\mu)$. All panels from Fig. 17 have been collapsed into a single distribution expressed as a function of reconstructed bin number. The dashed lines show the full uncertainty (statistical plus systematic) on the MC prediction.
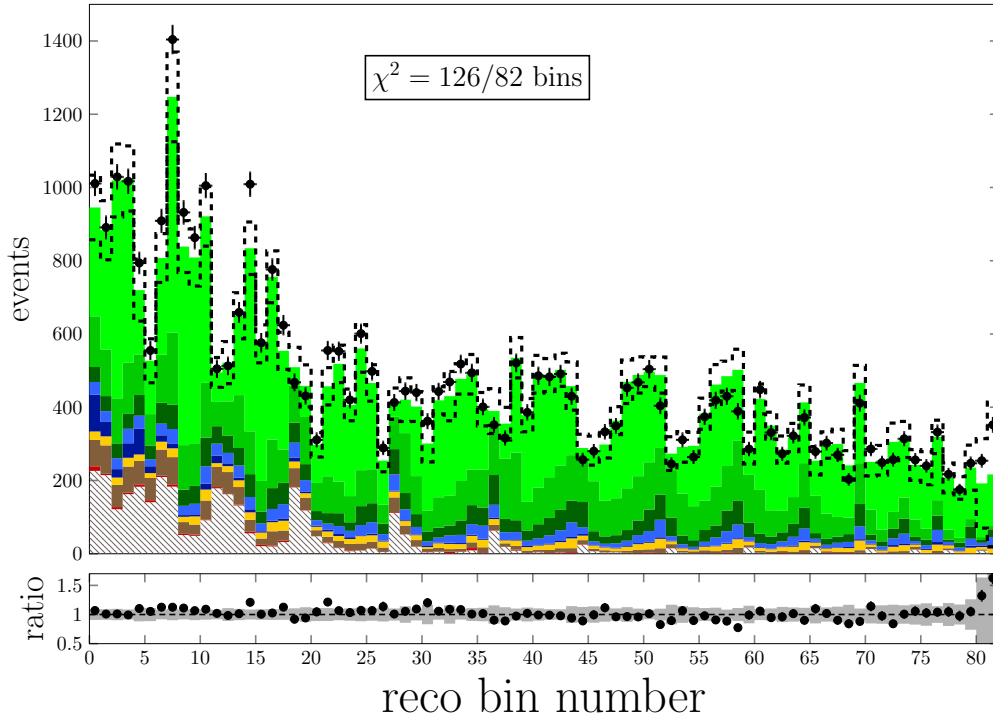
Figure 20: Summary plot for the full double-differential measurement of $(p_p, \cos\theta_p)$. All panels from Fig. 18 have been collapsed into a single distribution expressed as a function of reconstructed bin number. The dashed lines show the full uncertainty (statistical plus systematic) on the MC prediction.
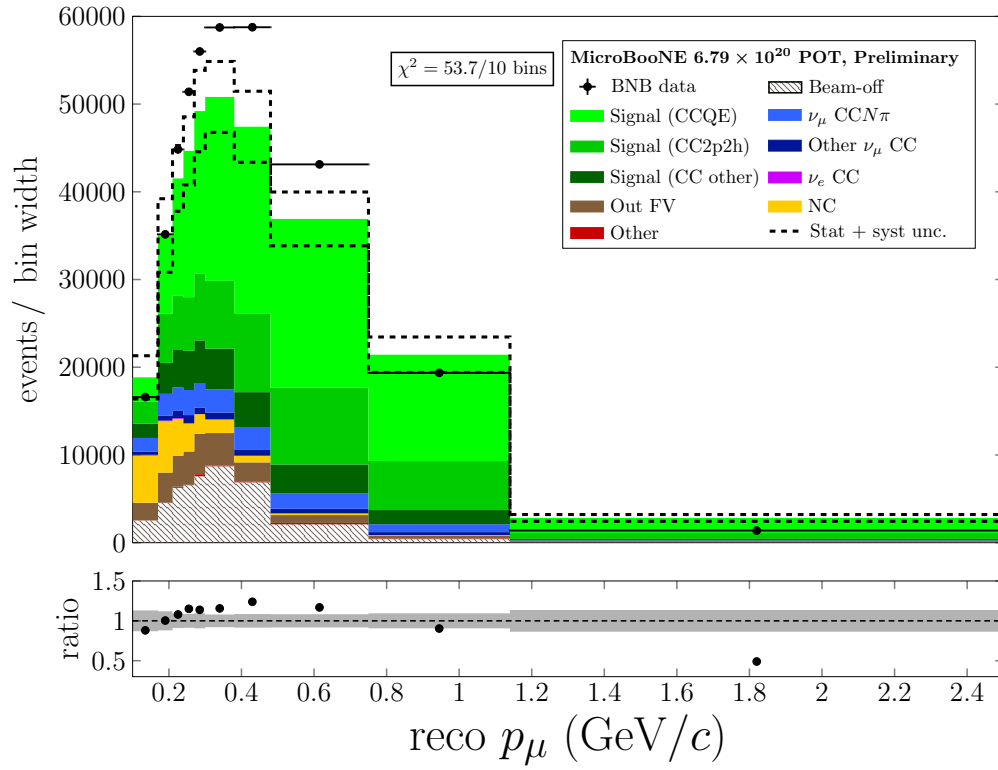
Figure 21: Single-differential measurement of p_μ obtained by integrating the 2D $(p_\mu, \cos\theta_\mu)$ event distribution over all angles. The dashed lines show the full uncertainty (statistical plus systematic) on the MC prediction.
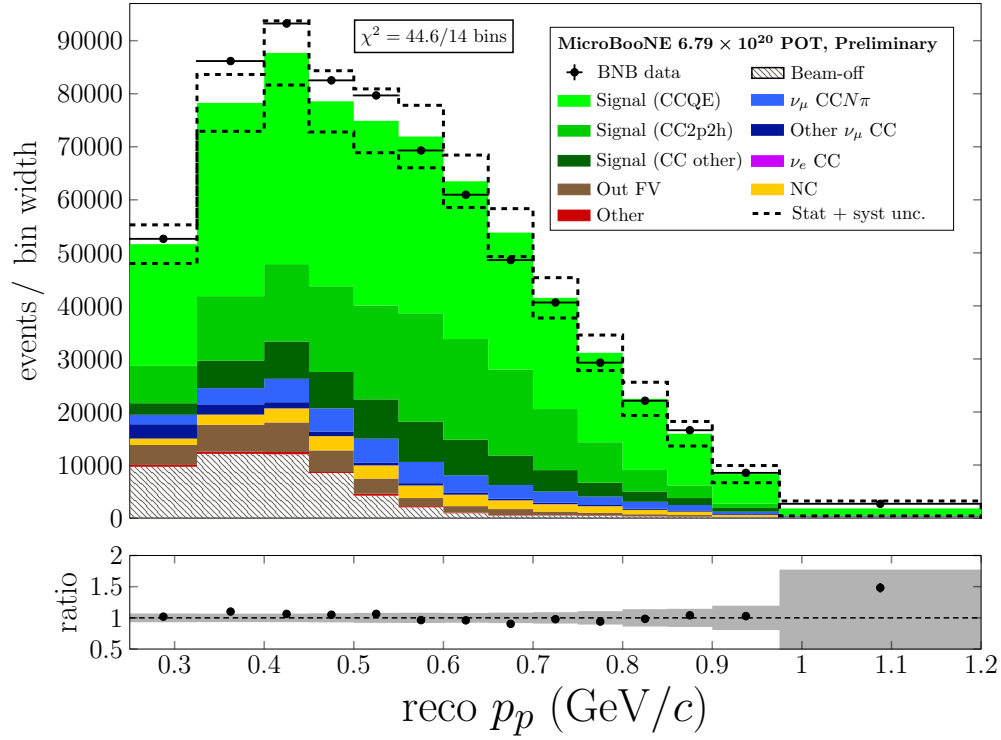
Figure 22: Single-differential measurement of p_p obtained by integrating the 2D $(p_p, \cos\theta_p)$ event distribution over all angles. The dashed lines show the full uncertainty (statistical plus systematic) on the MC prediction.
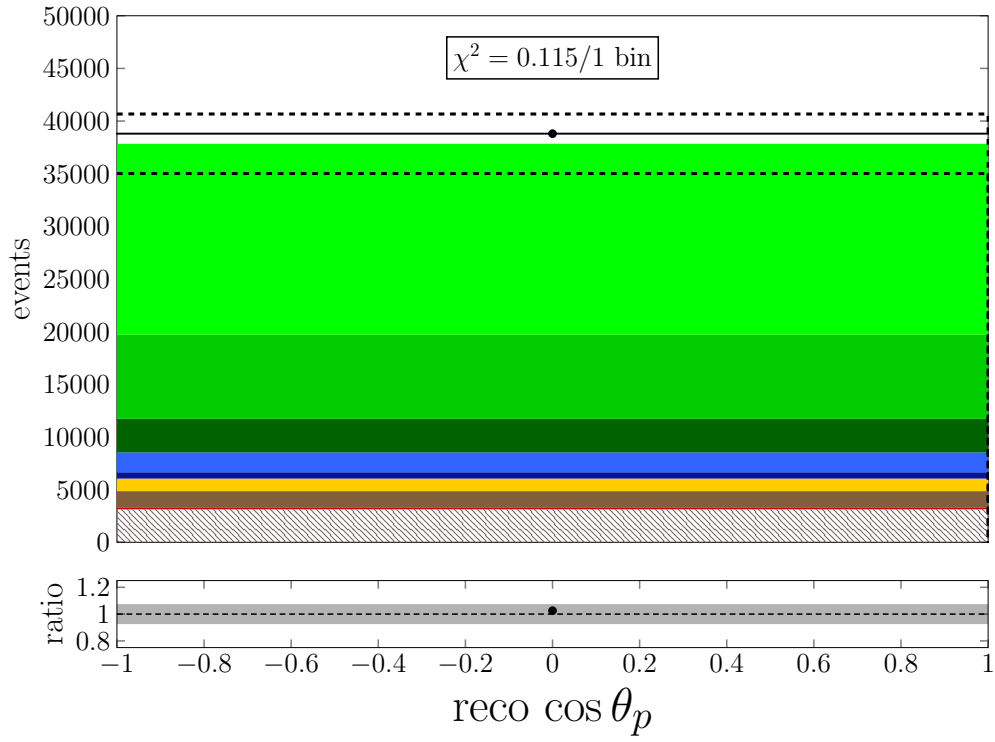
Figure 23: One-bin measurement of the total number of selected CC0πNp events. The dashed lines show the full uncertainty (statistical plus systematic) on the MC prediction.

8 Conclusions

The double-differential event rate measurements reported in this note lay the foundation for increasingly detailed MicroBooNE studies of the $CC0\pi Np$ interaction channel important for future precision neutrino oscillation measurements. The observed tensions between data and MicroBooNE MC predictions, shown here for joint distributions of momentum and scattering cosine for the muon and leading proton, present an opportunity for benchmarking theoretical calculations that will be fully realized with a near-future extraction of differential cross sections. Further explorations of $CC0\pi Np$ events in MicroBooNE have the potential to provide still greater sensitivity to challenging aspects of neutrino-nucleus interaction modeling, including correlations between the muon and leading proton and the multiplicity and kinematics of sub-leading protons.

The new results reported here, which build on a previous achievement of the first single-differential neutrino-argon cross-section measurement for the $CC0\pi Np$ channel [3], represent one aspect of MicroBooNE's continued progress in studying its world-leading neutrino-argon scattering dataset and in developing increasingly sophisticated simulation, reconstruction, and analysis tools for LArTPC detectors.

References

[1] P. A. Machado, O. Palamara and D. W. Schmitz, *The Short-Baseline Neutrino Program at Fermilab*, *Annu. Rev. Nucl. Part. Sci.* **69** (2019) 363 [1903.04608].

[2] DUNE collaboration, *Deep Underground Neutrino Experiment (DUNE), Far detector technical design report, Volume 1: Introduction to DUNE*, 2002.02967.

[3] MICROBOONE collaboration, *Measurement of differential cross sections for ν_μ-Ar charged-current interactions with protons and no pions in the final state with the MicroBooNE detector*, *Phys. Rev. D* **102** (2020) 112013 [2010.02390].

[4] MINIBOONE collaboration, *Significant excess of electronlike events in the MiniBooNE short-baseline neutrino experiment*, *Phys. Rev. Lett.* **121** (2018) 221801 [1805.12028].

[5] C. Andreopoulos, A. Bell, D. Bhattacharya, F. Cavanna, J. Dobson, S. Dytman et al., *The GENIE neutrino Monte Carlo generator*, *Nucl. Instrum. Methods Phys. Res. A* **614** (2010) 87.

[6] T2K collaboration, *Measurement of double-differential muon neutrino charged-current interactions on C_8H_8 without pions in the final state using the T2K off-axis beam*, *Phys. Rev. D* **93** (2016) 112012 [1602.03652].

[7] MICROBOONE collaboration, *Neutrino interaction model and uncertainties for MicroBooNE analyses*, MICROBOONE-NOTE-1074-PUB.

[8] MICROBOONE collaboration, *Booster neutrino flux prediction at MicroBooNE*, MICROBOONE-NOTE-1031-PUB.

[9] MINIBOONE collaboration, *Neutrino flux prediction at MiniBooNE*, *Phys. Rev. D* **79** (2009) 072002 [0806.1449].

[10] S. Agostinelli, J. Allison, K. Amako et al., *Geant4–a simulation toolkit*, *Nucl. Instrum. Methods Phys. Res. A* **506** (2003) 250.

[11] E. L. Snider and G. Petrillo, *LArSoft: toolkit for simulation, reconstruction and analysis of liquid argon TPC neutrino detectors*, *J. Phys.: Conf. Ser.* **898** (2017) 042057.

[12] D. Heck, J. Knapp, J. Capdevielle, G. Schatz and T. Thouw, *CORSIKA: A Monte Carlo code to simulate extensive air showers*, Tech. Rep. FZKA-6019, Institut für Kernphysik, feb, 1998. 10.5445/IR/270043064.

[13] W. Van De Pontseele, *Search for Electron Neutrino Anomalies with the MicroBooNE Detector*, Ph.D. thesis, Oxford University, 2020. 10.2172/1640226.

[14] R. Acciarri et al., *The Pandora multi-algorithm approach to automated pattern recognition of cosmic-ray muon and neutrino events in the MicroBooNE detector*, *Eur. Phys. J. C* **78** (2018) 82 [1708.03135].

[15] MICROBOONE collaboration, *Measurement of space charge effects in the MicroBooNE LArTPC using cosmic muons*, *J. Instrum.* **15** (2020) P12037 [2008.09765].

[16] MICROBOONE collaboration, *Calorimetric classification of track-like signatures in liquid argon TPCs using MicroBooNE data*, 2109.02460.

[17] MICROBOONE collaboration, *Determination of muon momentum in the MicroBooNE LArTPC using an improved model of multiple Coulomb scattering*, *J. Instrum.* **12** (2017) P10010 [1703.06187].

[18] L. Koch and S. Dolan, *Treatment of flux shape uncertainties in unfolded, flux-averaged neutrino cross-section measurements*, *Phys. Rev. D* **102** (2020) 113012 [2009.00552].

[19] F. Akbar, M. R. Alam, M. S. Athar, S. Chauhan, S. K. Singh and F. Zaidi, *Electron and muon production cross-sections in quasielastic $\nu(\bar{\nu})$-nucleus scattering for $E_\nu < 1$ GeV*, *Int. J. Mod. Phys. E* **24** (2015) 1550079.

[20] Y. Hayato, *A neutrino interaction simulation program library NEUT*, *Acta Phys. Pol. B* **40** (2009) 2477.

[21] J. Calcutt, C. Thorpe, K. Mahn and L. Fields, *Geant4Reweight: A framework for evaluating and propagating hadronic interaction uncertainties in Geant4*, *J. Instrum.* **16** (2021) P08042 [2105.01744].

[22] MICROBOONE collaboration, *Novel approach for evaluating detector systematics in the MicroBooNE LArTPC*, MICROBOONE-NOTE-1075-PUB.

[23] ARGONEUT collaboration, *A study of electron recombination using highly ionizing particles in the ArgoNeuT liquid argon TPC*, *J. Instrum.* **8** (2013) P08005 [1306.1712].

[24] MINIBOONE collaboration, *Neutrino flux prediction at MiniBooNE*, *Phys. Rev. D* **79** (2009) 072002 [0806.1449].